Journal of Materials Science & Technology 137 (2023) 36–55

Contents lists available at ScienceDirect

Journal of Materials Science & Technology

journal homepage: www.elsevier.com/locate/jmst

Research Article

Effect of mechanical ball milling on the electrical and powder bed properties of gas-atomized Ti–48Al–2Cr–2Nb and elucidation of the smoke mechanism in the powder bed fusion electron beam melting process

Seungkyun Yim, Kenta Aoyagi*, Keiji Yanagihara, Huakang Bian*, Akihiko Chiba

Institute for Materials Research, Tohoku University, 2-1-1 Katahira, Sendai, Miyagi 980-8577, Japan

ARTICLE INFO

Article history:
Received 11 May 2022
Revised 1 July 2022
Accepted 3 July 2022
Available online 20 August 2022

Keywords:
Metal–insulator transition
Electron beam melting additive manufacturing
Packing density
Flowability
Smoke mechanism
Percolation theory

ABSTRACT

Smoke is unexpected powder-splashing caused by electrostatic force and is one of the main problems hindering the process stability and applicability of the powder bed fusion electron beam (PBF-EB) technology. In this study, mechanical stimulation was suggested to suppress smoke of gas-atomized (GA) Ti–48Al–2Cr–2Nb powder using Al_2O_3 and WC ball milling. The deformation mechanism of the GA powder depending on the ball milling media was discussed based on the developed particle morphology distribution map and contact mechanics simulation. It was revealed that the rapid decrement of flowability and packing density after WC ball milling owing to the formation of angular fragments by the brittle fracture. The variation of surface and electrical properties by mechanical stimulation was investigated *via* XPS, TEM, and Impedance analysis. The electrical resistivity of the ball-milled powders gradually decreased with increasing milling duration, despite the increased oxide film thickness, and the capacitive response disappeared in Al-60 and WC-30 *via* metal–insulator transition. This could be due to the accumulation of strain and defects on the oxide film *via* mechanical stimulation. The smoke mechanism of ball-milled powders was discussed based on the percolation theory. In the smoke experiment, smoke was more suppressed for WC-10 and WC-20 than that for Al-40 and Al-50, respectively, despite the longer charge dissipation time. This could be due to the high probability of contact with conductive particles. For the Al-60 and WC-30 powders, smoke was further restricted by the formation of a percolation cluster with metal-like electrical conductivity. We believe that this study will contribute to a better understanding of the smoke mechanism and process optimization of the PBF-EB.

1. Introduction

Over the past decade, additive manufacturing (AM) techniques have been actively researched and developed, particularly in industrial fields. The high demand for AM techniques is attributed to their distinct advantages, including design freedom, short lead time, low material waste, and the distinctive microstructure of the product caused by rapid cooling [1]. In particular, the powder bed fusion electron beam (PBF-EB) method, an AM technique, has attracted considerable attention for fabricating non-weldable or brittle materials because it decreases the crack susceptibility [2,3]. The lower crack susceptibility originates from the distinctive building process of PBF-EB, in which the powder bed is preheated using a defocused electron beam to a high temperature at which the powder becomes slightly sintered. Then, the preheated powder bed is selectively melted using a high-voltage electron beam to produce a bulk part in a layer-by-layer manner. The high preheating temperature can reduce the residual stress to avoid distortion and failure of the final products built by PBF-EB [4].

However, unexpected powder scattering during the preheating process (which is known as the “smoke” phenomenon) limits the stability of the building process and the applicability of the PBF-EB technique [5]. During the preheating process, the irradiated electron beam is transferred through the powder bed into the base plate and then discharged through the ground wire. The powder feedstocks, such as Ni-based and Ti-based powders, generally have a core–shell structure, in which the surface of the powder is shielded by an insulating oxide film [5,6]. Thus, charge redis-

* Corresponding authors.
E-mail addresses: kenta.aoyagi.e7@tohoku.ac.jp (K. Aoyagi), huakang.bian.d5@tohoku.ac.jp (H. Bian).

https://doi.org/10.1016/j.jmst.2022.07.024
1005-0302/

tribution is blocked by the capacitive behavior of the dielectric layer, and charge can accumulate on the powder particles. During the preheating process, when the repulsive Coulomb force between the charged particles far exceeds the gravitational force, the powder feedstock splashes into the vacuum chamber from the powder bed, which is called smoke [7]. Smoke should be avoided because it leads to building termination through the complete removal of powder feedstock from the base plate.

Several studies have been conducted to explain the factors affecting smoke in the PBF-EB building process. Qi et al. reported that smoke can be affected by the momentum of the electrons and the electrostatic force [8]. Sigl et al. suggested three potential causes of smoke during the preheating process: water residue, the momentum of the electrons, and the electrostatic charge of the powder [9]. The electrostatic charge was identified as the predominant cause of smoke in the PBF-EB building process [9]. Cordero et al. demonstrated that powder bed smoke can be restricted by decreasing the charge dissipation time based on an analytical model [7]. Eschey et al. reported that the particle shape can affect the smoke probability, where the smoke in the preheating process was further suppressed using elongated powders compared to that using spherical powders [10]. However, the relationship between the powder bed properties and smoke probability remains unclear due to the difficulty of direct observation. Moreover, while pretreatment of the powder is an effective pathway to suppress smoke, it is challenging owing to the fine particle size and discrete nature of the powder.

In the previous study, mechanical stimulation was suggested to improve the electrical conductivity of Inconel 718 alloy powder, and the electrical resistivity of the powder was greatly reduced through ball milling [5]. More recently, it has been reported that the relaxation time of gas-atomized Ti–48Al–2Cr–2Nb powder was greatly reduced by mechanical ball milling, and smoke was restricted during the preheating process for ball-milled powders because of the decreased charge dissipation time [11]. However, the particle size and shape distributions of the gas-atomized Ti–48Al–2Cr–2Nb powder were significantly altered by ball milling. Because the effect of mechanical ball milling varies with the milling conditions and grinding media [12,13], the ball-milling conditions should be optimized to obtain a high packing density and good smoke suppression of the powder bed. Moreover, the relationship between the powder bed properties and smoke probability should be investigated to understand the smoke mechanism in detail.

The aim of this study is to investigate the effect of ball milling on the electrical and powder bed properties under various milling conditions. Gas-atomized Ti–48Al–2Cr–2Nb powder was ball-milled using Al_2O_3 and WC balls for various milling durations. The influence of the particle size and shape distributions on the flowability and packing density was analyzed. A spreading discrete element method (DEM) model was developed using the multi-sphere method to evaluate the packing density and coordination number of the ball-milled powders. The relationship between the smoke probability and powder bed properties was investigated based on percolation theory. Finally, a possible electrical circuit of ball-milled powders in the PBF-EB building process was suggested. This study provides a better understanding of the smoke mechanism and a possible method to suppress smoke in the PBF-EB building process.

2. Materials and methods

2.1. Mechanical ball milling and powder characterization

Gas-atomized (GA) Ti–48Al–2Cr–2Nb powder was prepared by Daido Steel Corp., Japan. The detailed chemical composition of the GA powder has been illustrated in the previous study [14]. Two types of milling media were used to manipulate the GA powder surface: (1) an Al_2O_3 ball (diameter of 5 mm) in an Al_2O_3 vessel and (2) a WC ball (diameter of 6 mm) in a WC vessel. The GA powder and each type of grinding ball (33.3 vol% each) were put in the milling vessel. Mechanical ball milling was conducted at 350 rpm for 10 to 60 min with an interval of 10 min in an air atmosphere using a planetary high-energy ball milling machine (Pulverisette 7, Fritsch GmbH, Germany).

The particle size distribution (PSD) of the powders was examined using a laser particle size analyzer (LS 230, Beckman Coulter, Inc., USA), and the particle morphology was observed using scanning electron microscopy (SEM, S-3400N, Hitachi High-Tech Science Corp., Japan). After ball milling, the area fraction of the deformed surface, which was characterized to a relatively smooth surface, was carefully measured *via* SEM image analysis (more than 300 particles) using the Zessis Axio-Vision microscope software following ASTM E562-11. To evaluate the morphological evolution after ball milling, a particle morphology distribution (PMD) map was constructed based on roundness (ϕ_R) and sphericity (ψ_S), as follows [15]:

$$\phi_R = 4\pi \cdot \frac{\text{Area}}{(\text{Perimeter})^2} = \frac{r_A}{r_P} \quad (1)$$

$$\psi_S = \frac{\text{Area}}{4\pi \times (\text{Major axis})^2} = \frac{r_A}{r_M} \quad (2)$$

where r_A, r_P, and r_M denote the computed particle radii based on the area, perimeter, and major axis, respectively. Thus, ϕ_R indicates the angularity of the particle surface, while ψ_S indicates the similarity of the particle shape to that of a sphere with the equivalent volume. Owing to considerable overlap of the data, 2D kernel density estimation was used to visualize the PMD map with the probability density function. The gravity-induced flowability of the powders was measured using a Hall flowmeter (JIS-Z2502, Tsutsui Scientific Instruments Co., Ltd., Japan) following ASTM B213. The crystal structures of the powders were investigated *via* X-ray diffraction (XRD, Philips X'PERT MPD, Malvern Panalytical, United Kingdom) with a Cu *Kα* source at 45 kV and 40 mA. The oxygen content of the powders was determined using an oxygen–nitrogen analyzer (ON736, Leco Corp., Japan).

2.2. XPS and TEM analyses

The surface composition of the powders was examined *via* XPS (PHI5000 VersaProbe II, ULVAC-PHI Inc., Japan) using a monochromatic Al *Kα* source (1486.7 eV) with a beam diameter of 50 μm. The powders were fixed on the carbon tape and then compressed using a manual hand press. The deformed surface was used to investigate the effect of mechanical stimulation on the surface properties. Survey and high-resolution spectra were collected to identify the following chemical elements: Ti (2*p*), Al (2*p*), Cr (2*p*), Nb (3*d*), and O (1*s*). The chemical composition of the particle surface was analyzed using the Common Data Processing System (Version 12). The XPS peak position was calibrated using the strong C 1*s* peak with a binding energy of 284.8 eV. To examine the oxide film thickness, thin films from the surfaces of the GA and ball-milled powders were prepared using a focused ion beam workstation (FIB, Helios NanoLab 600i, FEI Company, USA). Before the FIB treatment, the particle surface was coated with platinum to protect it from the electron beam. The oxide film thickness of the powders was examined using scanning transmission electron microscopy (STEM, Titan^{3TM} 60–300 with a double corrector, FEI Company, USA).

2.3. Electrical property analysis and smoke tests

The direct current (DC) resistivity of the powders was measured using a customized electrical measurement system under a

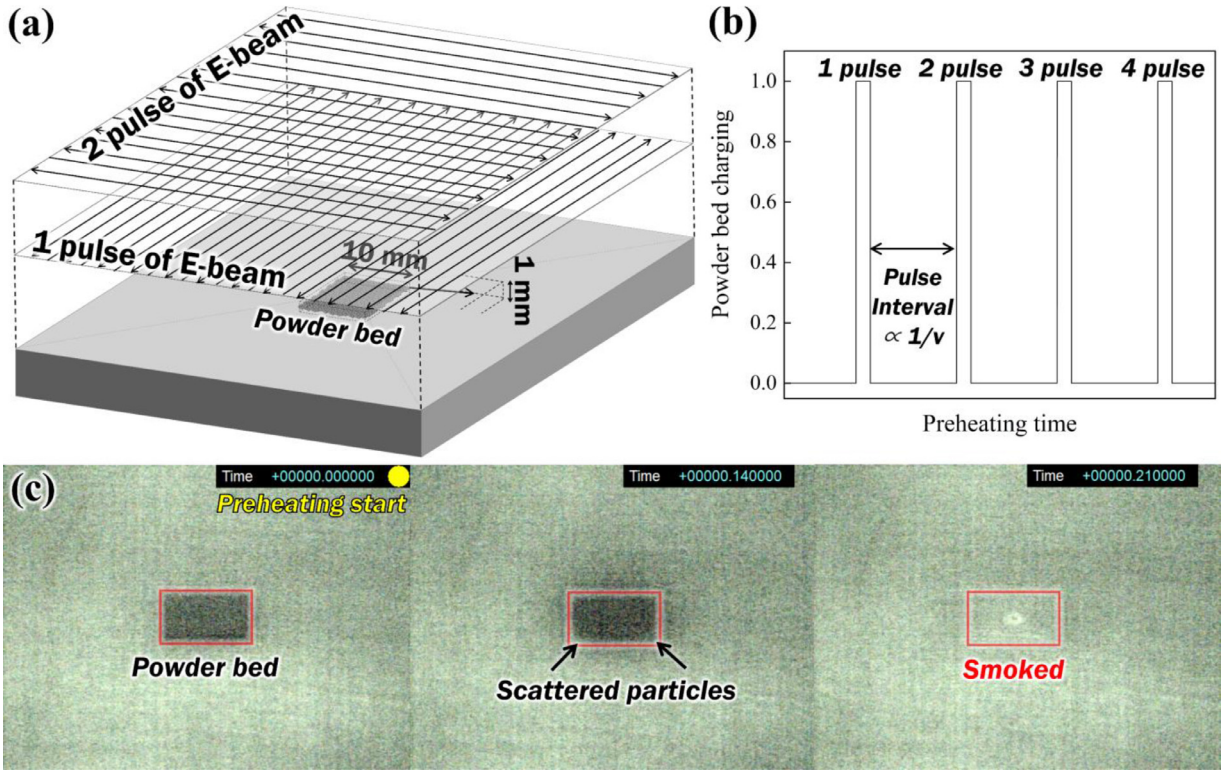

Fig. 1. Schematics of the smoke test during preheating of the PBF-EB building process: (a) powder bed with the scan strategy, (b) time dependence of the repeated electron beam pulse, and (c) high-speed camera images during the smoke test.

vacuum environment (<5.0 × 10^{-4} Pa). The bulk powders of approximately 2.5 g were placed inside an Al_2O_3 tube (diameter of 10 mm), and the top and bottom of the powder were sealed by upper and bottom electrodes (diameter of 10 mm). Subsequently, the powder was compressed by an upper punch with the compressive force of 7 N to retain a constant contact area between the particles in each measurement. To investigate the frequency-dependent electrical properties of the powders (such as resistance, capacitance, and inductance), impedance spectroscopy analysis was conducted between 1 Hz and 2 MHz using an inductance–capacitance–resistance (LCR) meter (ZM 2376 LCR, NF Corp., Japan). The details of the measurement method can be found in a previous study [5].

The smoke probability was investigated *via* the pulse repetition method using a JEOL PBF-EB machine (JBS-Z0100EBM, JEOL Ltd., Japan), as shown in Fig. 1. The powder was placed in a machined square hole (10 × 10 × 1 mm^3) in the center of the base plate and then recoated using a stainless-steel comb to remove the excess powder. The packing density (ρ_{PB}) of the powders was estimated using the mass of the deposited powder at least five times, as follows:

$$\rho_{PB} = \frac{m_{PB}}{V_H} \times \frac{100}{\rho_t} \tag{3}$$

where m_{PB} is the mass of the deposited powder bed, V_H is the volume of the machined square hole, and ρ_t is the true density of the Ti–48Al–2Cr–2Nb alloy (3.979 g/cm^3). Preheating was conducted in a snake pattern using electron beam with a beam current of 5 mA, scan pitch of 2 mm, and scan speed of 200 to 350 m/s (Fig. 1(a)). During the smoke test, the powder bed was repeatedly charged by a traveling electron beam, whose pulse interval was inversely proportional to the scan speed (Fig. 1(b)). Smoke occurrence was validated more than three times using a high-speed camera with a framerate of 250 frames/s (Fig. 1(c)).

2.4. Contact mechanics simulation

The contact mechanics model for the collision between the grinding ball and a single Ti–48Al–2Cr–2Nb particle was developed based on a finite element framework [16]. The contact radius (r_c) between the grinding ball and Ti–48Al–2Cr–2Nb particle can be expressed as [17]

$$r_c = \left(\frac{3F}{8} \cdot \frac{R^*}{E^*}\right)^{\frac{1}{3}} \tag{4}$$

where F is the applied impact force, E^* is the equivalent modulus, and R^* is the equivalent radius. E^* and R^* can be expressed as

$$\frac{1}{E^*} = \frac{1-\nu_g^2}{E_g} + \frac{1-\nu_p^2}{E_p} \tag{5}$$

$$\frac{1}{R^*} = \frac{1}{R_g} + \frac{1}{R_p} \tag{6}$$

where E_g and E_p are the Young's moduli, ν_g and ν_p are the Poisson's ratios, and R_g and R_p are the radii of the grinding ball and Ti–48Al–2Cr–2Nb particle, respectively. The pressure variation in the contact region can be expressed as

$$p = \frac{3F}{2\pi r_c^2}\left\{1 - \left(\frac{r_d^2}{r_c^2}\right)\right\}^{\frac{1}{2}} \tag{7}$$

where r_d is the distance from the center of the contact surface. The total indentation depth (d) can be expressed as

$$d = \left(\frac{9}{16} \cdot \frac{F^2}{R^* E^{*2}}\right)^{\frac{1}{3}} \tag{8}$$

The parameters for contact mechanics finite element simulation are listed in Table 1.

Table 1
Parameters for the contact mechanics simulation.

Parameter	WC ball	Al_2O_3 ball	Ti–48Al–2Cr–2Nb
Particle diameter	6 mm	5 mm	71 μm
Density (g/cm^3)	15.63	3.91	3.789
Poisson's ratio	0.21	0.21	0.24
Young's modulus (GPa)	650	365	220

Table 2
Parameters for the spreading DEM simulation.

Parameter	Ti–48Al–2Cr–2Nb
Density (g/cm^3)	3.979
Poisson's ratio	0.31
Young's modulus, E (GPa)	220
Surface energy, γ (mJ)	0.0103
Normal coefficient of restitution, e_n	0.35
Shear coefficient of restitution, e_s	0.22
Sliding friction coefficient, μ_s	0.531
Rolling friction coefficient, μ_r	0.234
Damping coefficient	0.112

2.5. Discrete element method simulation

Experimental characterization of particle interactions in a powder bed is difficult because of their discrete nature and local accumulation of numerous particles. DEM is one of the available pathways for investigating the interactions of many discrete particles ($>10^3$). In this study, a spreading DEM model was developed to simulate the powder bed for smoke testing using the open-source YADE framework [18]. The Hertz–Mindlin contact model combined with the Derjaguin–Muller–Toropov (DMT) model was used to simulate the particle flow during the powder deposition process. The particle interactions were considered as physical contact between two elastic particles, and the contact force was determined using Hertzian contact theory [17]. This assumption is acceptable because the metallic particles are not plastically deformed during the spreading process. The detailed equation can be found in the previous study [14]. The multi-sphere approach was implemented to approximate the elongated particle shape according to the ψ_S distribution with an interval of 0.1. The parameters (Table 2) for the spreading DEM model were fixed to clarify the influence of the PSD and ψ_S distribution.

3. Results

3.1. The particle size distribution and particle morphology distribution variation

The particle morphology and microstructure of the GA powder are presented in Fig. 2. The raw powder consisted of spherical particles with several satellites, and the surface exhibited a coarse texture (Fig. 2(a) and (b)). In the cross-sectional images, a dendritic microstructure composed of α_2-Ti_3Al and γ-TiAl was observed, and the surface was covered with a thin oxide film (Fig. 2(c)–(e)). In a previous study, it was confirmed that the electrical resistance of Inconel 718 and Ti–48Al–2Cr–2Nb powders was significantly reduced by mechanical stimulation using ball milling [5,11]. In this study, to investigate the influence of grinding media on the electrical and surface properties of the powder, mechanical ball milling was performed using Al_2O_3 and WC balls at 350 rpm for up to 60 min. The physical and electrical properties of the GA powder changed only slightly after Al_2O_3 ball milling for up to 30 min; thus, these shorter milling times were not considered in this study. For simplicity, the powders mechanically ball-milled using the Al_2O_3 ball for 40, 50, and 60 min are denoted as Al-40, Al-50, and Al-60, respectively. Similarly, the powders ball-milled using the WC ball for 10, 20, and 30 min are denoted as WC-10, WC-20, and WC-30, respectively.

The PSDs and mean diameters of the powders are presented in Fig. 3. The PSD of the GA powder gradually widened after Al_2O_3 ball milling with increasing milling duration, while the mean particle diameter decreased because of the consistent decrease in the d10 and d90 values (Fig. 3(a) and (c)). Compared to that after Al_2O_3 ball milling, PSD broadening was more significant after WC ball milling, despite shorter milling durations (Fig. 3(b)). The mean particle diameter decreased up to WC-20, while it increased for WC-30 because of the increase in d90 (>100 μm). This result suggests that pulverization was dominant in WC ball milling for up to 20 min, while agglomeration became dominant for longer durations (30 min).

The PMD maps of the powders are shown in Fig. 4. The colored probability density can be standardized using a shape-classification chart, as shown in Fig. 4(a). The shape factor (k) representing the surface irregularity of the powder was defined using linear regression analysis: $y = kx + b$. As shown in Fig. 4(b), the GA powder was mainly composed of spherical particles ($\psi_S > 0.8$). The fraction of elongated particles ($\psi_S < 0.8$) and shape factor of the GA powder were calculated to be 0.204 and 0.544, respectively. Compared to that after Al_2O_3 ball milling, the fraction of elongated particles rapidly increased after WC ball milling, despite the shorter milling time. The shape factor decreased to 0.422 after Al_2O_3 ball milling for 40 min, and then increased after Al_2O_3 ball milling for 50 min or longer. It should be noted that ϕ_R of Al_2O_3 ball-milled powders was lower than that of the GA powder, indicating a smoother surface. In contrast, the shape factor gradually increased after WC ball milling with increasing milling duration, indicating a more angular surface.

Images of the particle surface and the deformed area fractions (f_d) of the powders are shown in Fig. 5. After Al_2O_3 ball milling for 40 min (Al-40), the textured surface of the GA powder changed to a relatively smooth surface, and the surface-attached satellites were eliminated (indicated by the green arrows in Fig. 5(a)). This suggests that the decrease in the shape factor after Al_2O_3 ball milling was due to the removal of surface-attached satellites through continuous pulverization. After WC ball milling for 10 min (WC-10), the surface satellites were removed, while several angular fragments were observed owing to brittle fracture of the particles. This indicates that the increased shape factor after WC ball milling was due to the formation of angular fragments. Compared to that of the Al_2O_3 ball-milled powders, f_d rapidly increased for the WC ball-milled powders with increasing milling duration owing to the formation of fresh surfaces (Fig. 5(g) and (h)).

To clarify the different mechanisms of Al_2O_3 and WC ball milling, the contact force caused by the collision between the grinding ball and a single GA particle was examined using the developed contact mechanics model (Fig. 6(a)). The applied impact force of the grinding ball during ball milling can be expressed as [19]

$$F(t) = 4\pi^2 m_g \upsilon_m^2 \left\{ r_d^2 + r_v^2 + 2 r_d r_v \cos[2\pi (i+1)\upsilon t] \right\}^{\frac{1}{2}} \quad (9)$$

where m_g is the weight of the grinding ball, υ_m is the rotation speed of the milling vessel (rad/s), r_d is the radius of the main disk, and r_v is the internal radius of the milling vessel. The maximum impact force of the WC ball was calculated to be 1.15, which is 0.19 higher than that of the Al_2O_3 ball because of its higher weight (Fig. 6(b)). The maximum von Mises stresses caused by collision with the Al_2O_3 and WC balls were determined to be 1369 and 5549 MPa, respectively (Fig. 6(c) and (d)). The maximum deformation depths of the GA powder were estimated using the yield strength of the TiAl alloy (~400 MPa) to be 15 and 48 μm from collision with the Al_2O_3 and WC balls, respectively (Fig. 6(e) and (f)). This indicates that the severe deformation after WC ball

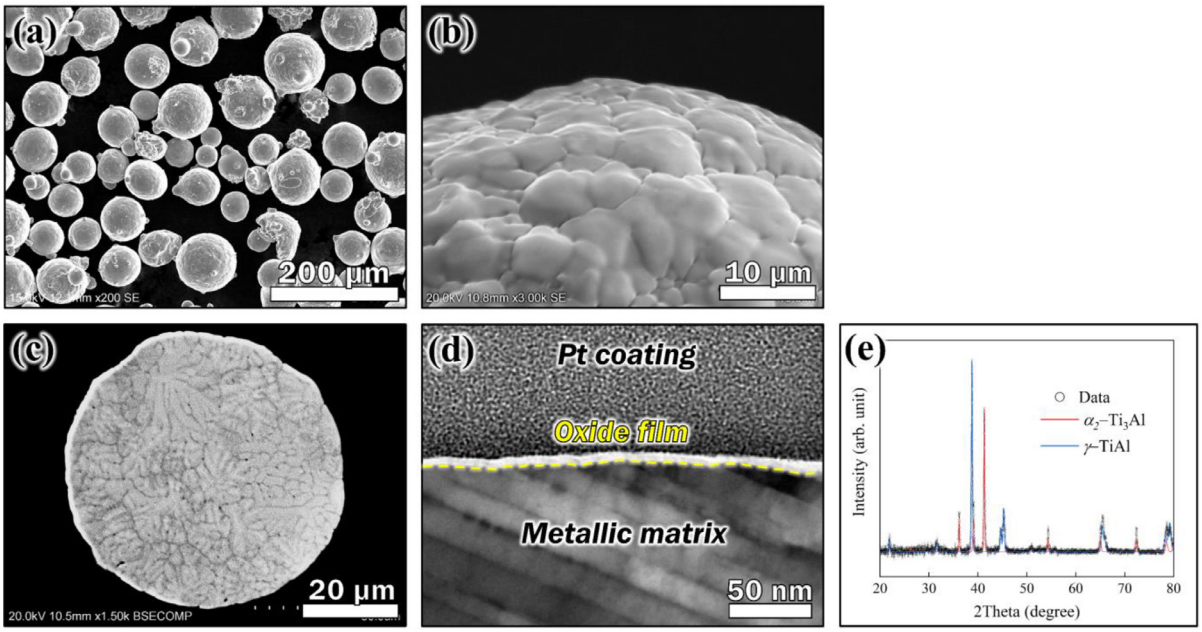

Fig. 2. Microstructure of the gas-atomized Ti–48Al–2Cr–2Nb powder: (a), (b) SEM images of the surface, (c) backscattered electron image of the cross section, (d) dark-field TEM image, and (e) XRD pattern.

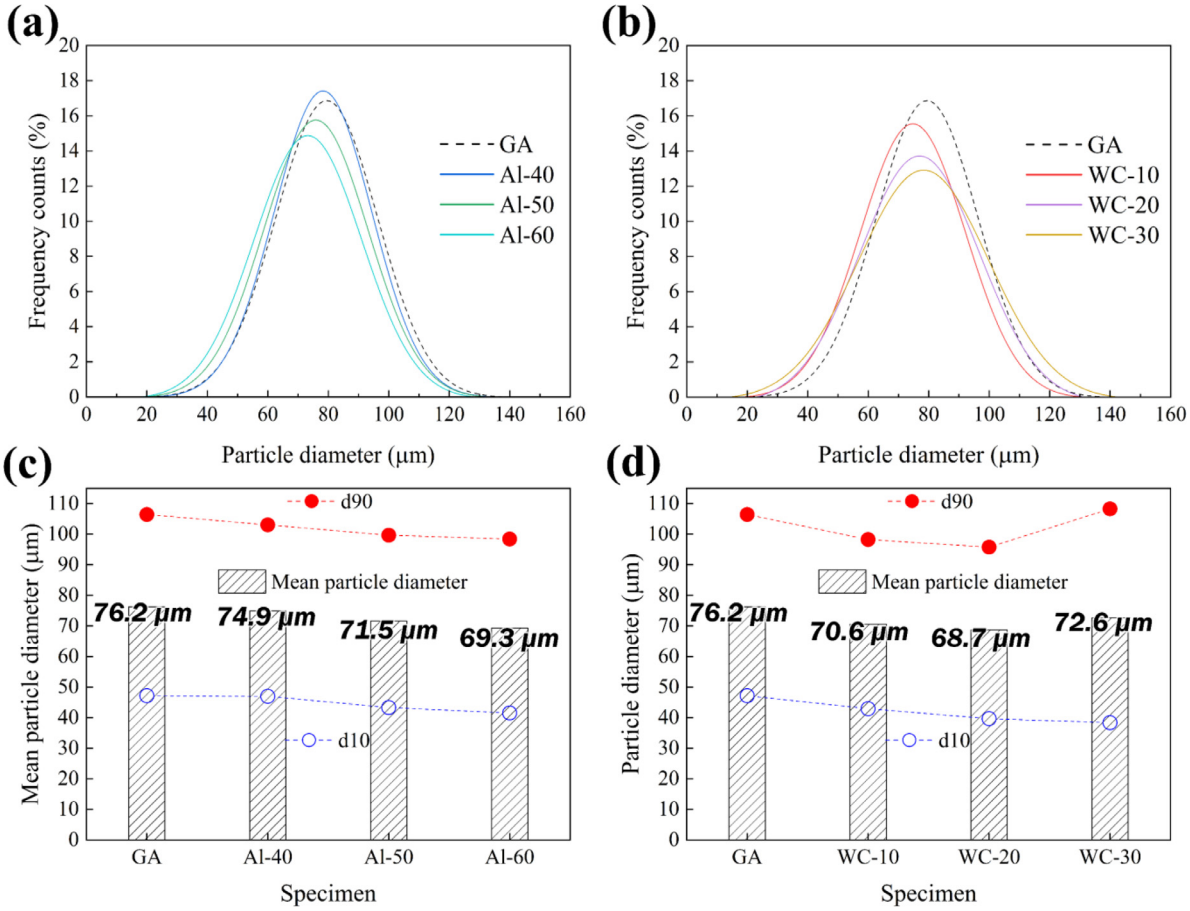

Fig. 3. Particle size distributions and mean particle sizes of the Ti–48Al–2Cr–2Nb powders: (a), (c) GA and Al_2O_3 ball-milled powders and (b), (d) GA and WC ball-milled powders.

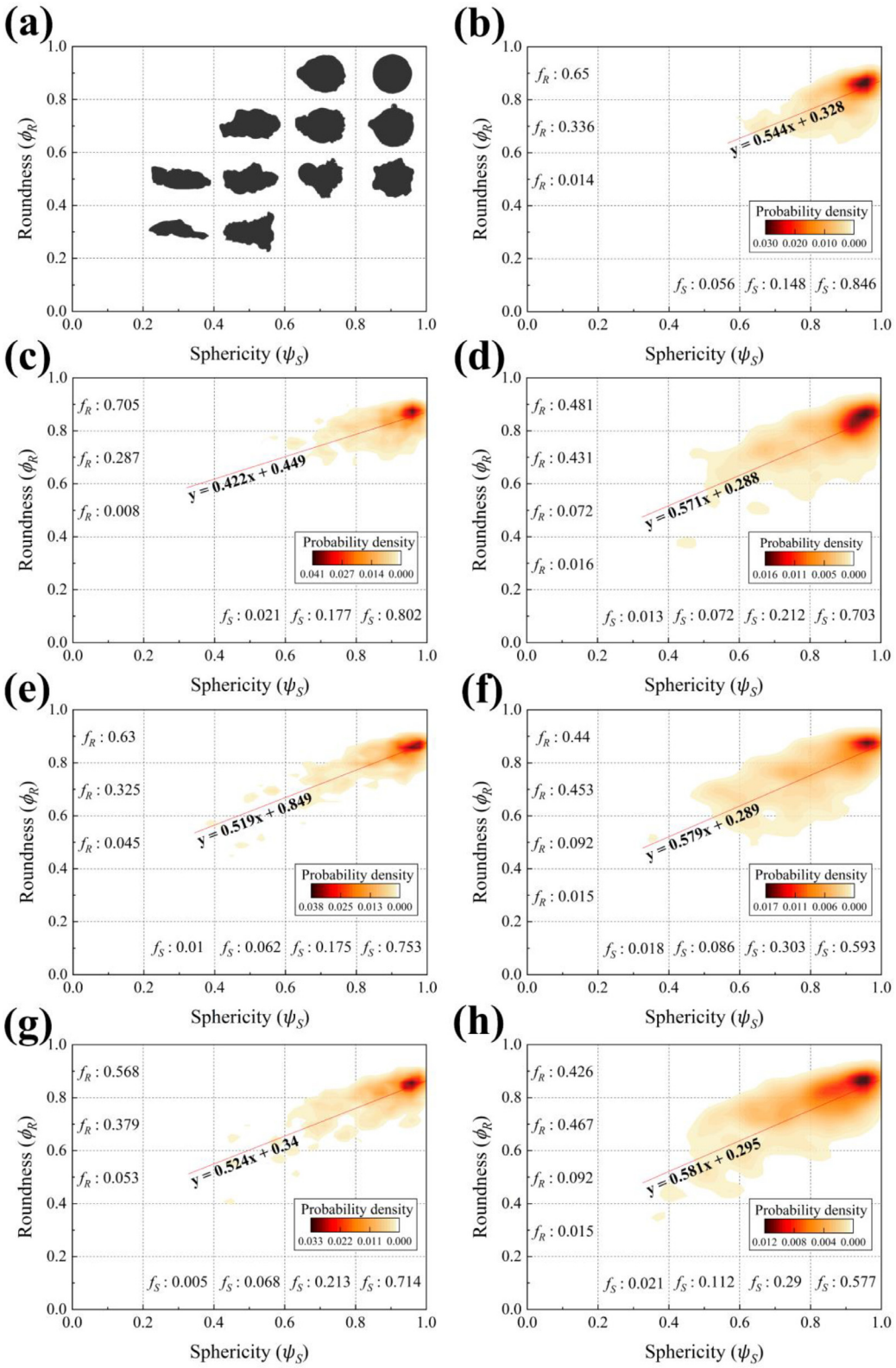

Fig. 4. Particle morphology distribution maps of the Ti–48Al–2Cr–2Nb powders: (a) shape classification chart, (b) GA, (c) Al-40, (d) WC-10, (e) Al-50, (f) WC-20, (g) Al-60, and (h) WC-30 (red lines represent the linear regression plot).

milling was due to the high supplied contact force originating from the high weight of the grinding ball.

The mass flow rate measured by Hall flowmeter and packing density of the powders are shown in Fig. 7. The mass flow rate of the GA powder decreased slightly after Al_2O_3 ball milling with increasing milling duration, while it decreased rapidly after WC ball milling, despite the relatively short milling time. Interestingly, the mass flow rate of WC-10 (1.39 g/s) was considerably lower than that of Al-60 (1.45 g/s), despite their similar PSDs and fractions of elongated particles (Fig. 4(d) and (g)). In contrast, the packing

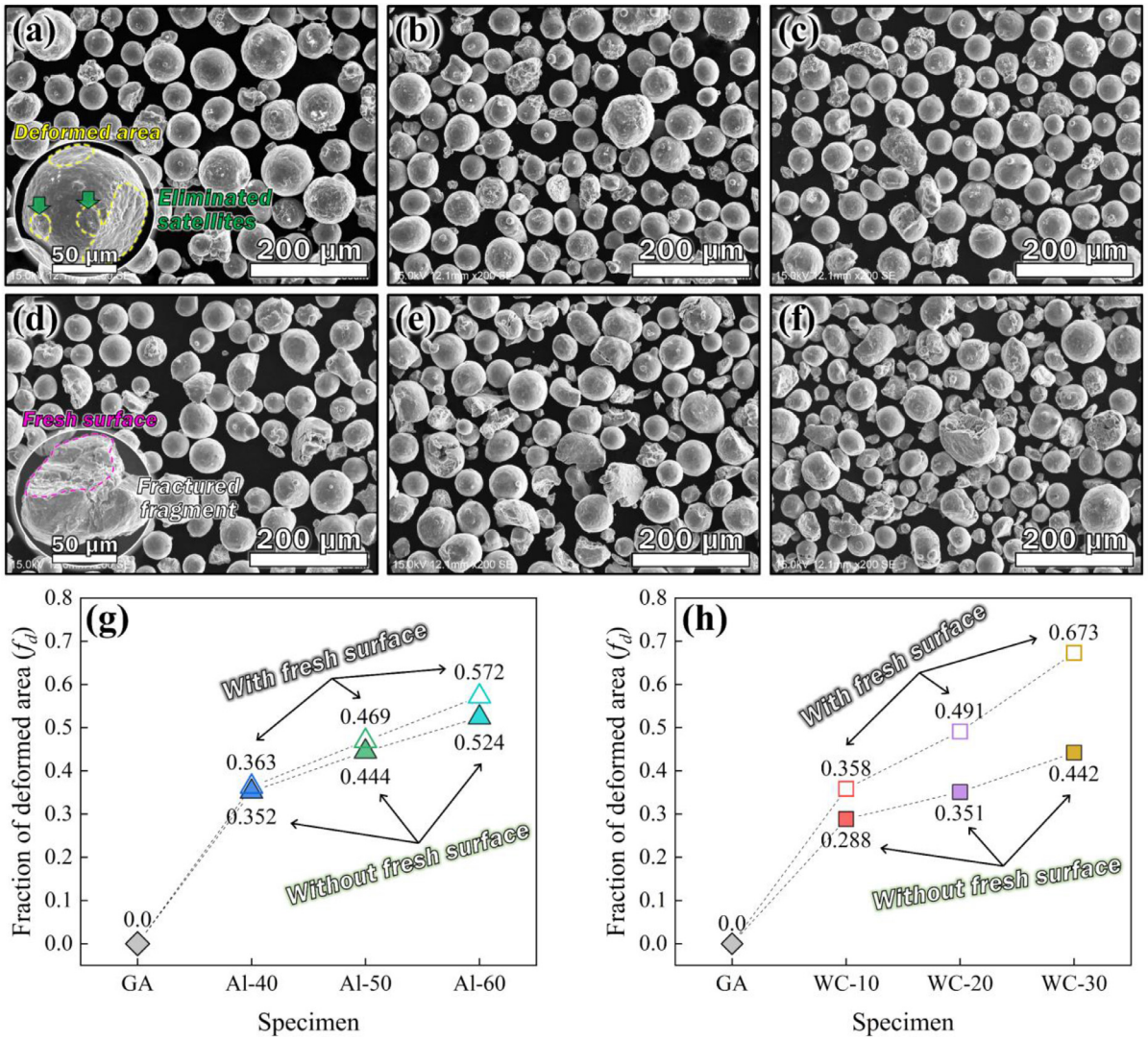

Fig. 5. SEM images of the Ti–48Al–2Cr–2Nb powders: (a) Al-40, (b) Al-50, (c) Al-60, (d) WC-10, (e) WC-20, and (f) WC-30. Area fractions of the deformed surface: (g) Al_2O_3 and (h) WC ball-milled powders.

density increased after Al_2O_3 ball milling with increasing milling duration, while it consistently decreased after WC ball milling.

3.2. Surface characterization of the ball-milled powders

Dark-field TEM images and the corresponding oxygen element distributions of the powders are presented in Fig. 8. The oxide film thickness of the GA powder was approximately 6.5 nm, and the metallic matrix directly below the oxide film consisted of wide α_2 and thin γ plates, which followed the Blackburn orientation relationship of $\{111\}\gamma//(0002)\alpha_2$ and $<110>\gamma//<11\bar{2}0>\alpha_2$ [20]. Based on the oxygen distributions, the oxide film thicknesses of the Al-40 and WC-10 powders were estimated to be 12.6 and 9.1 nm, respectively. As the milling duration increased, the oxide film thickness increased considerably to 42.3 nm (Al-60) and 101.1 nm (WC-30) owing to oxygen contamination. In the oxygen content analysis, the oxygen concentration of Al-60 was higher than that of WC-30 owing to a longer ball milling duration (Table 3). Moreover, the metallic matrix near the oxide films of Al-60 consisted of single grain, while that of WC-30 consisted of several fine grains. This result indicates that the oxide layer formation *via* ball milling needs sufficient strain and defects accumulation for reducing the energetic cost for oxidation. Therefore, extended oxide film *via* ball milling could be consisted of fine crystallites due to the defects and strain accumulation, as shown in Fig. 8(d) and (e).

Table 3
Oxygen concentration of the GA and ball-milled powders (wt%).

GA	Al-40	Al-50	Al-60	WC-10	WC-20	WC-30
0.063	0.105	0.141	0.168	0.0921	0.105	0.111

The surface chemical states of the powders were characterized *via* XPS analysis and are presented in Fig. 9. The survey spectra of the GA and ball-milled powders were similar, indicating similar surface chemical compositions (Fig. 9(a) and (b)). The detailed chemical composition was examined using the high-resolution deconvolved Ti 2*p*, Al 2*p*, Cr 2*p*, Nb 3*d*, and O 1*s* spectra. The oxide films of the powders were mainly composed of Al_2O_3 and TiO_2, and the composition changed slightly after ball milling (Table 4). In the Ti 2*p* spectra, the GA powder exhibited TiO_2 and metallic Ti peaks, and the metallic Ti peak disappeared after ball milling (Fig. 9(c) and (d)). Similarly, the intensity of the metallic Al peak of the GA powder decreased with increasing milling duration (Fig. 9(e) and (f)). This could be due to the increased oxide film thickness after ball milling, which impeded X-ray pene-

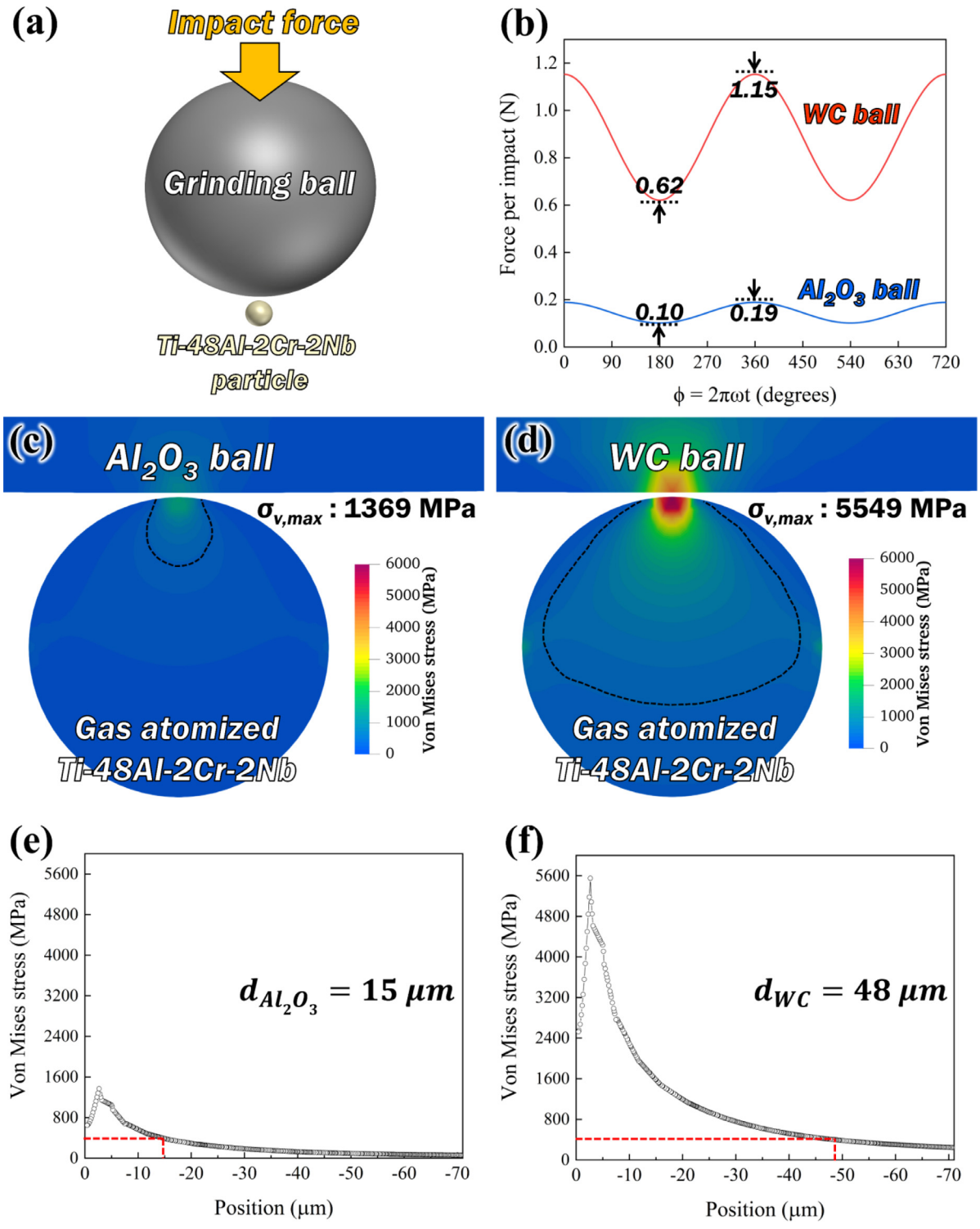

Fig. 6. (a) Schematic of the contact mechanics simulation and (b) force per impact of the Al_2O_3 and WC balls. Snapshot images and corresponding deformation depths of the Ti–48Al–2Cr–2Nb powder after collision with the (c), (e) Al_2O_3 and (d), (f) WC balls.

tration to the metallic matrix [21]. In contrast, the intensities of Ti_nO_{2n-1}-type suboxide peaks, such as TiO and Ti_2O_3, increased with increasing milling duration, while the intensity of the O^{2-} peak decreased owing to the formation of Ti_nO_{2n-1}-type suboxides (Table 4). This result suggests that the oxide film can be partially reduced by ball milling, even under an air atmosphere.

The XPS spectra near the valence band region of the powders are presented in Fig. 10(a) and (b). The valence band maxima of the powders were similar, near 3.74 eV. An elongated valence band tail representing metal-like conductivity was observed in the GA powder. As mentioned previously, the metallic matrix peaks in the Ti 2*p* and Al 2*p* spectra were caused by X-ray penetration into the matrix owing to the very thin oxide film (~6.5 nm). Therefore, the elongated valence band tail of the GA powder was due to the contribution of the metallic matrix. The valence band tail rapidly decreased with the increasing oxide film thickness in the

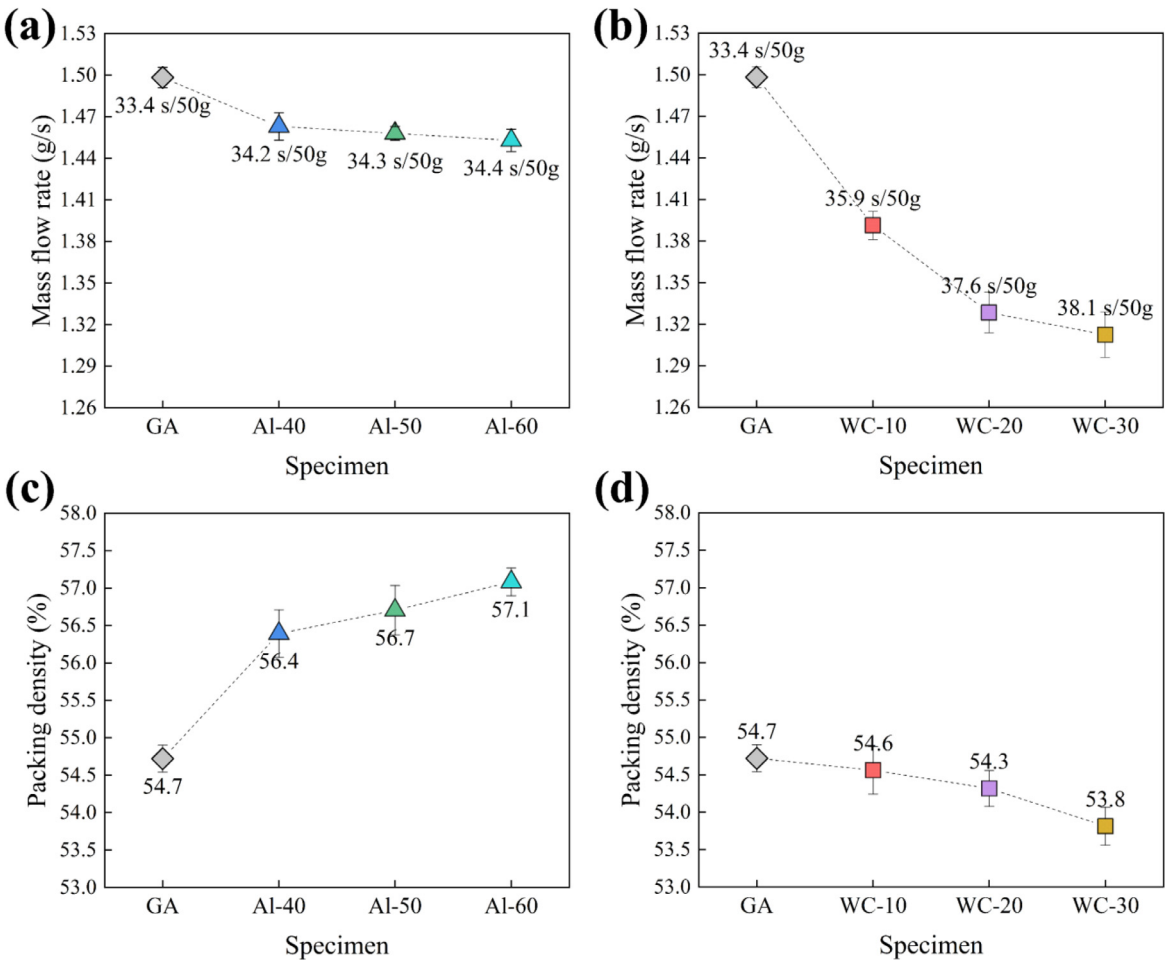

Fig. 7. Gravity-induced mass flow rate and packing density of the Ti–48Al–2Cr–2Nb powders: (a), (c) GA and Al_2O_3 ball-milled powders and (b), (d) GA and WC ball-milled powders.

Table 4
Surface chemical compositions of the GA and ball-milled powders.

Specimen	Atomic concentration of oxide surface (at%)						
	O^{2-}	Ti^{4+}	Ti^{3+}	Ti^{2+}	Al^{3+}	Cr^{3+}	Nb^{5+}
GA	65.86	8.49	0.95	0.49	23.01	0.86	0.35
WC-10	65.02	9.99	1.39	0.53	22.30	0.44	0.32
WC-20	64.11	9.79	1.52	0.98	22.47	0.71	0.43
WC-30	60.26	8.77	1.86	1.89	26.22	0.57	0.43
Al-40	65.21	9.39	1.27	0.62	22.21	0.82	0.48
Al-50	64.26	8.91	1.44	0.80	23.07	0.98	0.54
Al-60	60.03	8.41	2.26	1.04	27.07	0.76	0.43

Al-40 and WC-10 powders, while it increased as the milling duration increased further, despite the increased oxide film thickness. Interestingly, the valence band tails of Al-60 and WC-30 are comparable to that of the metallic material.

3.3. The direct current and alternating current (AC) electrical properties of the ball-milled powders

The DC resistivities of the powders at room temperature are shown in Fig. 11(a) and (b). The electrical resistivity of the GA powder was 1.92×10^4 Ω m, which is similar to that of a dielectric material. This could be due to the synergistic effect of the insulating oxide film and the extremely small contact area between the spherical particles. The electrical resistivity decreased by approximately 1/3 for the Al-40 and WC-10 powders, despite the expanded oxide film, and it was almost six orders of magnitude lower for Al-60 and WC-30, which is similar to that of metallic materials.

The AC impedance results of the powders are shown in Fig. 12. In the Nyquist plot, the real parts of the impedance in the low- and high-f_{AC} ranges represent the ohmic (R_m) and oxide film (R_o) resistances, respectively. For the GA powder, R_o was approximately 766 kΩ, and it decreased after ball milling to 161 and 167 kΩ for Al-40 and WC-10, respectively (Fig. 12(a)). In the Bode plots of the GA, Al-40, and WC-10 powders, an almost −45° slope in the intermediate f_{AC} range was observed, representing the characteristics of the passive oxide film, and the maximum phase angle was approximately −90°, indicating an ideal capacitor (Fig. 12(c) and (d)). However, the maximum phase angles of Al-40 and WC-10 were slightly shifted toward higher f_{AC} values, indicating rapid charge dissipation compared to that of the GA powder at a phase angle of 45° [22]. As the milling duration increased, the R_o values of Al-50 and WC-20 rapidly decreased to approximately 42 and 97 Ω (Fig. 12(b)), respectively. From the Bode plot, the maximum phase angles of Al-50 and WC-20 decreased to −15° and −30°, respectively, indicating degradation of the capacitive characteristics (Fig. 12(f)). The R_o values of Al-60 and WC-30 decreased considerably to 5 and 3 Ω, respectively, despite the increased oxide film thickness, and the peak phase angles decreased to 25° and 50°, respectively, representing an inductive response (Fig. 12(f)). This indicates that the oxide film of the GA powder transitioned from capacitive to inductive, exhibiting metallic-like electrical conductivity in the Al-60 and WC-30 powders.

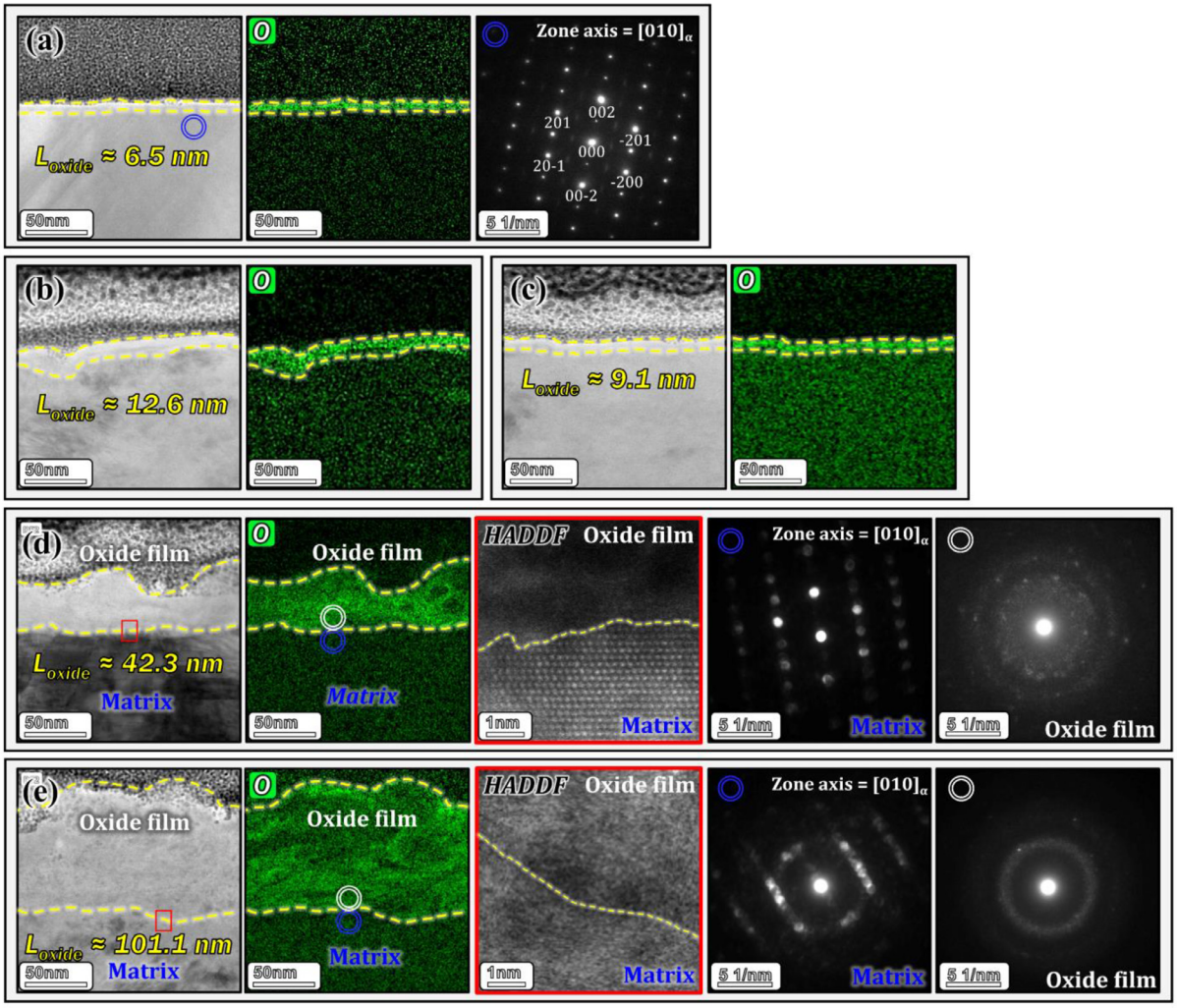

Fig. 8. Dark-field TEM images, the oxygen maps, and diffraction patterns of the Ti–48Al–2Cr–2Nb powders: (a) GA, (b) Al-40, (c) WC-10, (d) Al-60, and (e) WC-30.

3.4. Electrostatic force and smoke test during the preheating process

The ideal relaxation processes in a parallel resistor–capacitor (R–C) circuit can be expressed by Kirchhoff's current law [23]:

$$I_R + I_C = \frac{V}{R} + C\frac{dV}{dt} \tag{10}$$

$$V(t) = V_0 \exp\left(-\frac{\tau}{RC}\right) \tag{11}$$

where V_0 is the applied voltage at $\tau = 0$, and τ is the time constant representing the dielectric relaxation or charge dissipation time. Using the impedance data, the τ of the R–C circuit can be expressed as

$$\tau = \frac{1}{\omega_p} = \frac{1}{2\pi f_{AC,p}} \tag{12}$$

where $f_{AC,p}$ is the peak frequency from the Bode plot. The detailed impedance data is presented in Table 5. Generally, the number of phase angle peaks in the Bode plot represents the number of relaxation processes, and the phase angle peaks can overlap when the relaxation time scales are similar [23]. To simplify the calculation, the R–C circuit of the powders was assumed to be a single R–C circuit. The calculated τ values of the powders are shown in Fig. 13(a). The τ value of the GA powder was 265.3 μs, and it decreased after ball milling to 49.7 and 58.6 μs for the Al-40 and WC-10 powders, respectively. As the milling duration increased further, the τ values decreased substantially to 0.095 and 0.099 μs for the Al-50 and WC-20 powders, respectively, and it disappeared for Al-60 and WC-30 owing to the formation of the inductive layer exhibiting metal-like electrical conductivity. The electrostatic force (F_{ES}) between two contacting particles, which mainly affects the smoke during the preheating process, can be calculated by [7]

$$F_{ES} = \frac{{Q_C}^2}{16\pi\varepsilon_0 {r_i}^2} \cdot f_\xi \tag{13}$$

where Q_C is the charging degree of the particles, ε_0 is the vacuum permittivity, r_i is the equivalent radius of particle, and f_ξ is a nu-

Table 5
Impedance spectroscopy results of the GA and ball-milled powders.

Sample	R_{metal} (Ω)	R_{oxide} (Ω)	$f_{AC,p}$ (Hz)	ω_{Max}	τ (μs)
GA	92	765,950	600	3770	265.258
A-40	92	161,249	3200	20,106	49.736
A-50	23	42	1.68×10^6	10.6×10^6	0.095
A-60	3	5	1.38×10^6	8.7×10^6	–
W-10	95	167,036	2700	16,965	58.946
W-20	58	97	1.83×10^6	10.0×10^6	0.99
W-30	2	3	1.24×10^6	7.8×10^6	–

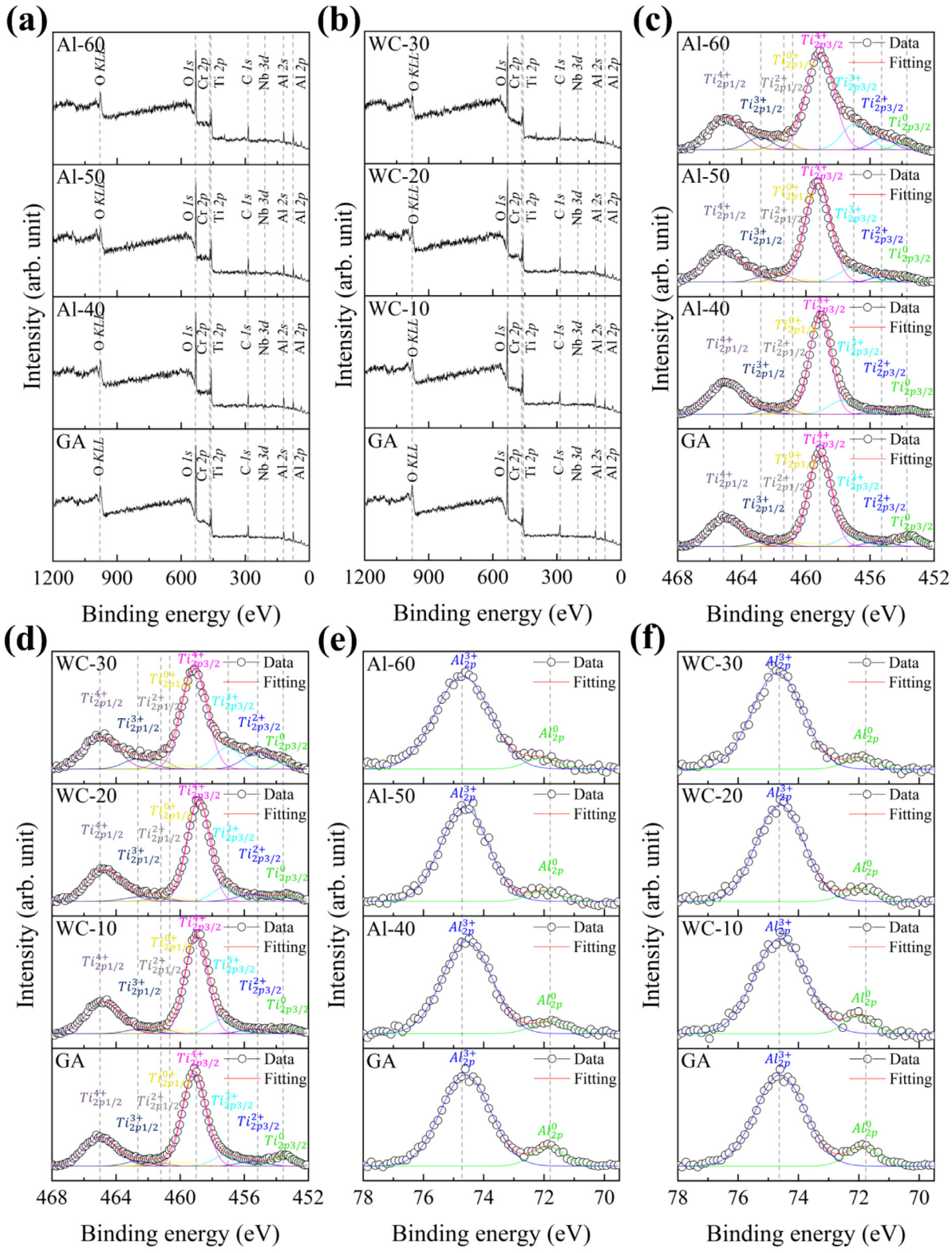

Fig. 9. (a), (b) XPS survey spectra of the Ti–48Al–2Cr–2Nb powders. High-resolution XPS spectra of (c), (d) Ti 2p, (e), (f) Al 2p. (a), (c), and (e) correspond to the GA and Al_2O_3 ball-milled powders, whereas (b), (d), and (f) correspond to the GA and WC ball-milled powders.

merical geometry-dependent function. Q_C can be expressed as

$$Q_C = J\pi {r_i}^2 \eta \tau \left(\frac{1 - e^{-\frac{\Delta t}{\tau}}}{1 - e^{-\frac{T}{\tau}}} \right) \quad (14)$$

where J is the input current density from the e-beam, η is the absorption efficiency, and T is the raster time of the preheating area. For the calculation, the preheating parameters were set to be $J = 50.66$ kA/m^2, beam diameter = 200 μm, scan speed = 200 m/s, and $\eta = 0.9$. The calculated electrostatic forces of the powders are

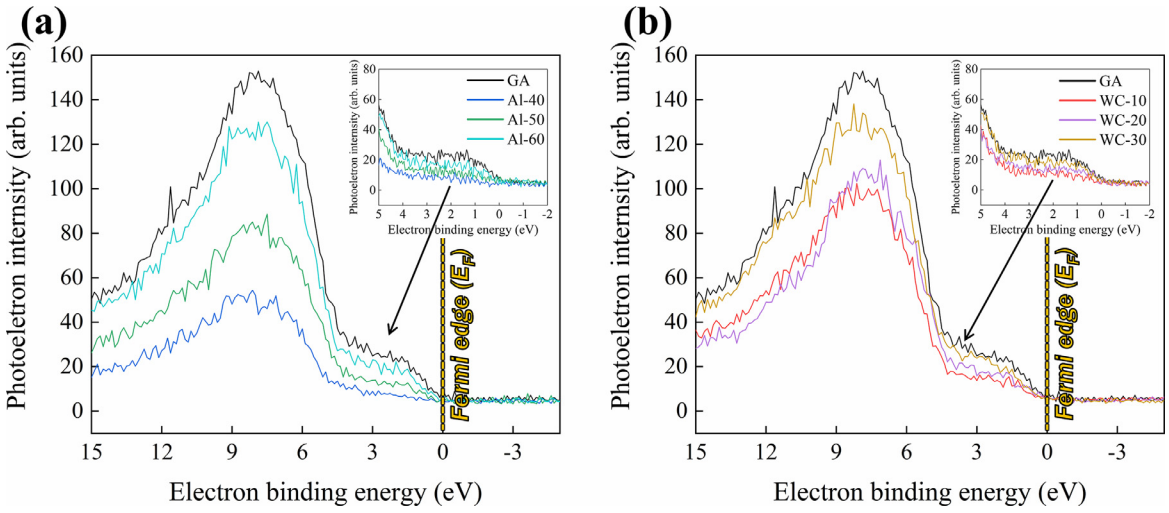

Fig. 10. XPS spectra near the valence band region of the Ti–48Al–2Cr–2Nb powders: (a) GA and Al_2O_3 ball-milled powders and (b) GA and WC ball-milled powders.

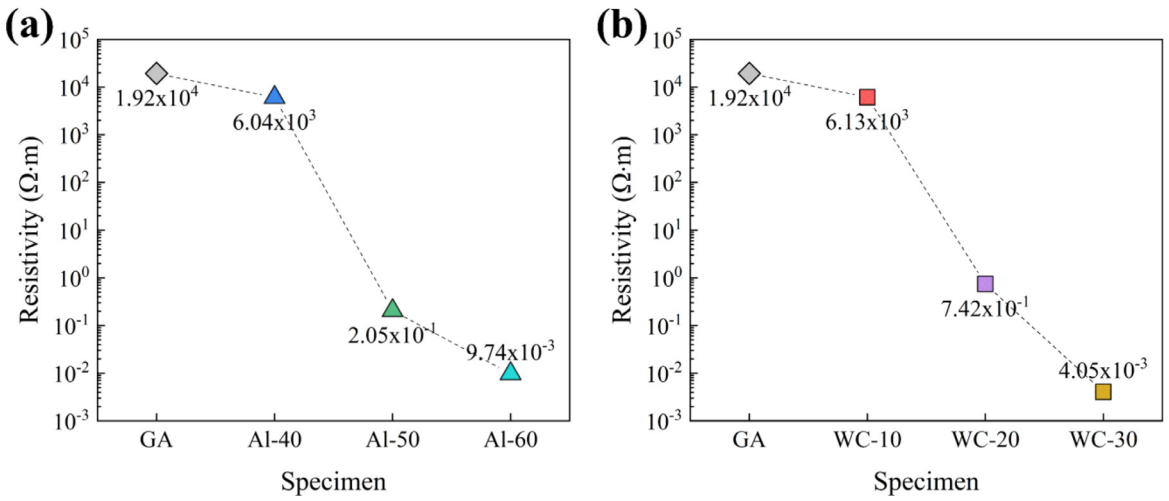

Fig. 11. Room-temperature DC resistivities of the Ti–48Al–2Cr–2Nb powders: (a) GA and Al_2O_3 ball-milled powders and (b) GA and WC ball-milled powders.

shown in Fig. 13(b). The F_{ES} value of the GA powder decreased with increasing milling duration because of the reduced charge dissipation time. Comparing the powders with time constants on the same scale, the F_{ES} value of Al-40 was lower than that of WC-10, and the F_{ES} value of Al-50 was lower than that of WC-20, indicating that smoke was less likely to occur for Al_2O_3 ball-milled powder under the same preheating conditions.

The experimentally verified smoke probabilities of the powders during the preheating process are presented in Fig. 14(a) and (b). Smoke occurred in the GA powder bed for scan speeds above 250 m/s, while it was prevented in the Al-40 and WC-10 powder beds owing to the decreased charge dissipation time. Interestingly, the smoke probability of Al-40 at 300 m/s was higher than that of WC-10, despite the lower charge dissipation time. As the milling duration increased further, smoke was prevented for Al-50 for scan speeds of up to 300 m/s, and it was prevented for scan speeds of up to 350 m/s for WC-20. This result does not match the trend of the charge dissipation time and the predicted electrostatic force. Thus, it can be deduced that there are other factors that significantly influence powder bed smoke in the PBF-EB building process. The smoke was completely prevented at a scan speed of 350 m/s for the Al-60 and WC-30 powders, where it was preheated above 900 °C by manipulating the beam current. Therefore, it is confirmed that mechanical ball milling is an effective method for inhibiting smoke for the Ti–48Al–2Cr–2Nb alloy in the PBF-EB building process.

3.5. Electron trajectory simulation during preheating process

A Monte Carlo simulation was conducted to determine the interaction between the irradiated electron beam and powder bed. A snapshot of the electron beam trajectory with the GA powder bed is shown in Fig. 15(a). The mean energy loss model for the accelerated electrons was established using the following equation [24]:

$$E_{i+1} = E_i - \frac{\mathrm{d}E}{\mathrm{d}S} \cdot L_i \tag{15}$$

$$-\frac{\mathrm{d}E}{\mathrm{d}S} = \frac{-4\pi e^4}{m_0 c^2 \beta_i^2} N_0 \rho \sum_{i=1}^{n} \frac{C_i Z_i}{A_i} \left[\ln\left(\frac{297.91\beta_i^2}{f_i}\right) - \ln\left(1-\beta_i^2\right) - \beta_i^2 \right] \tag{16}$$

where E_i is the kinetic energy of an irradiated electron at point i, L_i is the distance between two elastic collisions, $-\mathrm{d}E/\mathrm{d}S$ is the rate of energy loss according to Bethe's equation, m_0c^2 is the rest energy of the primary electron, β_i is the ratio of the speed of the electron to that of light, N_0 is Avogadro's number, and C_i, Z_i, A_i, and f_i are the weight fraction, atomic number, atomic weight, and

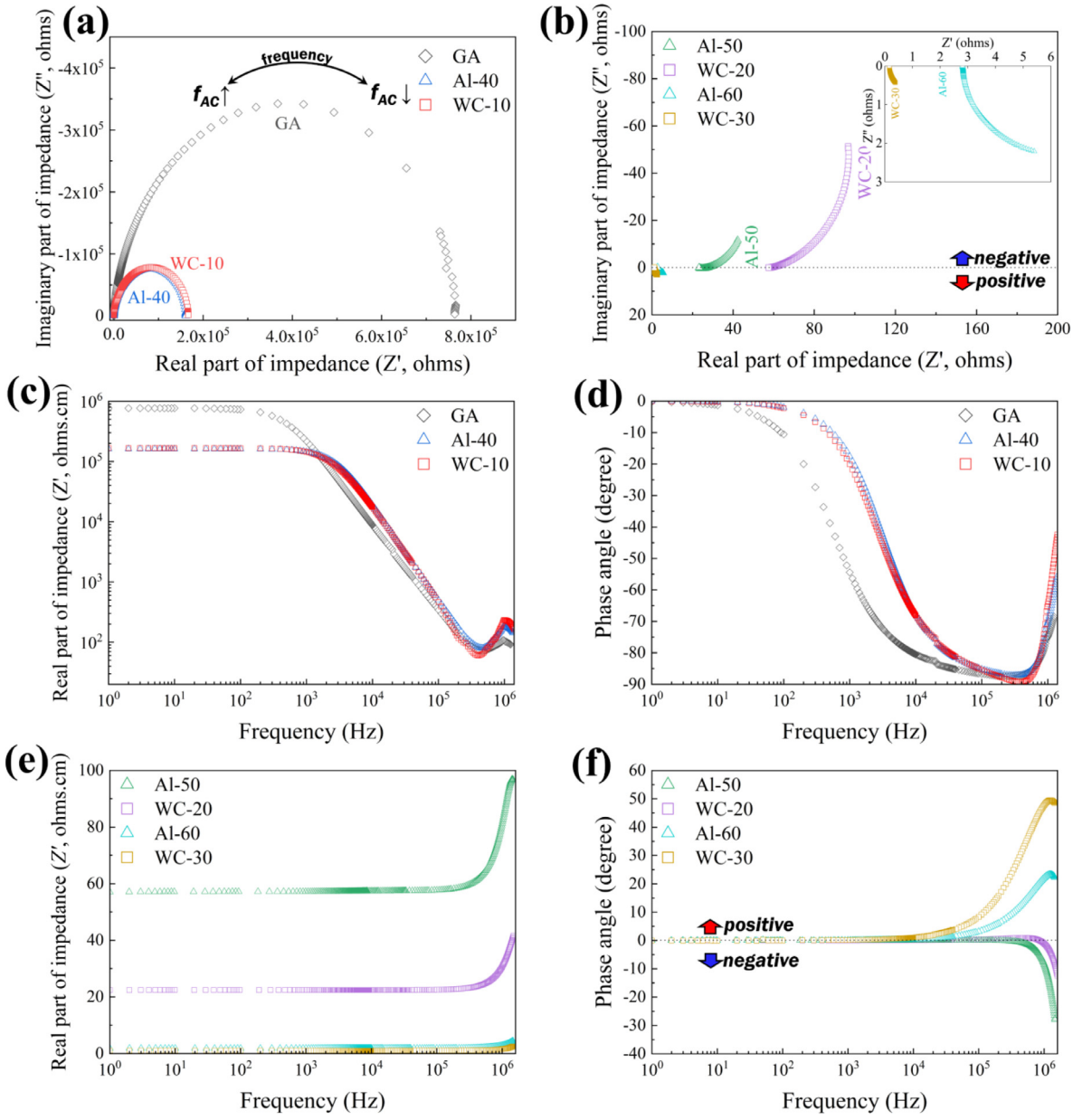

Fig. 12. Impedance spectroscopy results of the GA and ball-milled Ti–48Al–2Cr–2Nb powders: (a), (b) Nyquist plots and (c), (d), (e), (f) Bode plots.

mean ionization potential of element *i*, respectively. In this model, free electrons were accelerated to 60 keV and then irradiated into the deposited powder bed with a beam diameter of 200 μm. The deposited GA powder bed was assumed to comprise spherical particles with a diameter of 71 μm, which were stacked in a face-centered cubic structure. When the electron beam struck the GA powder bed, the kinetic energy of the electrons was converted into heat energy by multiple elastic and inelastic collisions with the lattice atoms in an arbitrary direction, while a certain number of electrons were backscattered into the vacuum atmosphere. In this simulation, the backscattering coefficient (η) was determined to be 0.186 (Fig. 15(b)). The electrons were continuously scattered until they lost their kinetic energy and were trapped in the lattice atoms of the powder particles. As shown in Fig. 15(c) and (d), most of the electrons were trapped in the GA powder bed within a width of 160 μm and penetration depth of 90 μm. This result indicates that electrical charging initially occurred in the upper powder bed region during the preheating process.

3.6. Powder bed properties from the discrete element method (DEM) simulation

The packing density and coordination number of the powder bed were investigated based on the developed spreading DEM model. A typical example of the powder deposition process for the smoke test is shown in Fig. 16. The multi-sphere method was implemented to imitate the non-spherical particles according to the ψ_S distribution with an interval of 0.1. Firstly, a loose sphere pack without contacts between particles was generated based on the corresponding PSD to imitate the powder pouring for the smoke test (Fig. 16(a)), and arbitrary spherical particles were replaced with clump particles according to the corresponding f_s (Fig. 16(b)). The replaced clump pack was deposited into a square hole ($1 \times 1 \times 1$ mm^3) *via* the raindrop method by gravitational force (Fig. 16(c)). Subsequently, a stainless-steel comb traveled along the y-direction with a velocity of 500 mm/s to fill the square hole with a flat surface (Fig. 16(d)).

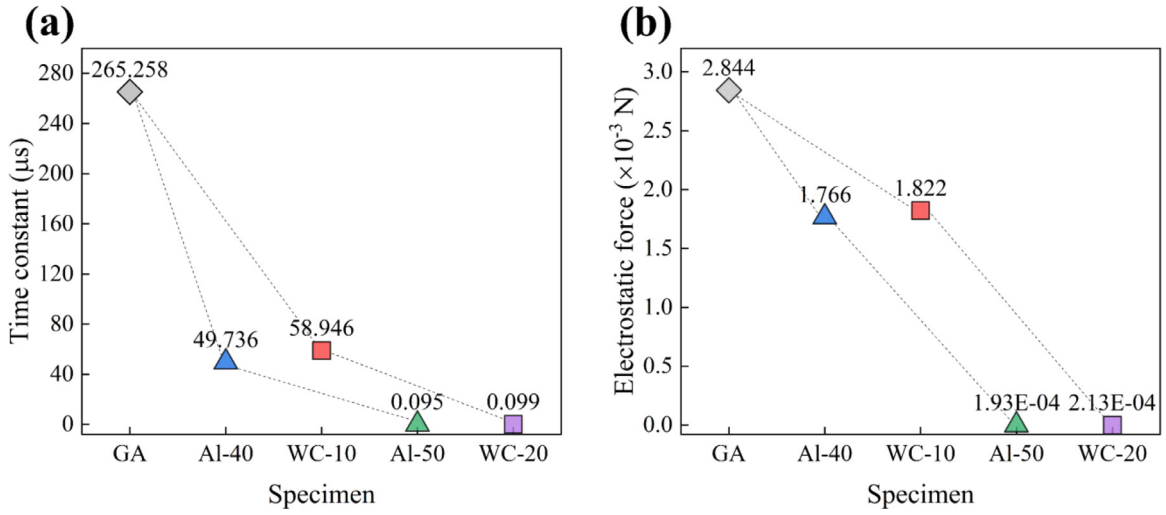

Fig. 13. Calculated (a) time constants and (b) electrostatic forces of GA, Al-40, Al-50, WC-10, and WC-20.

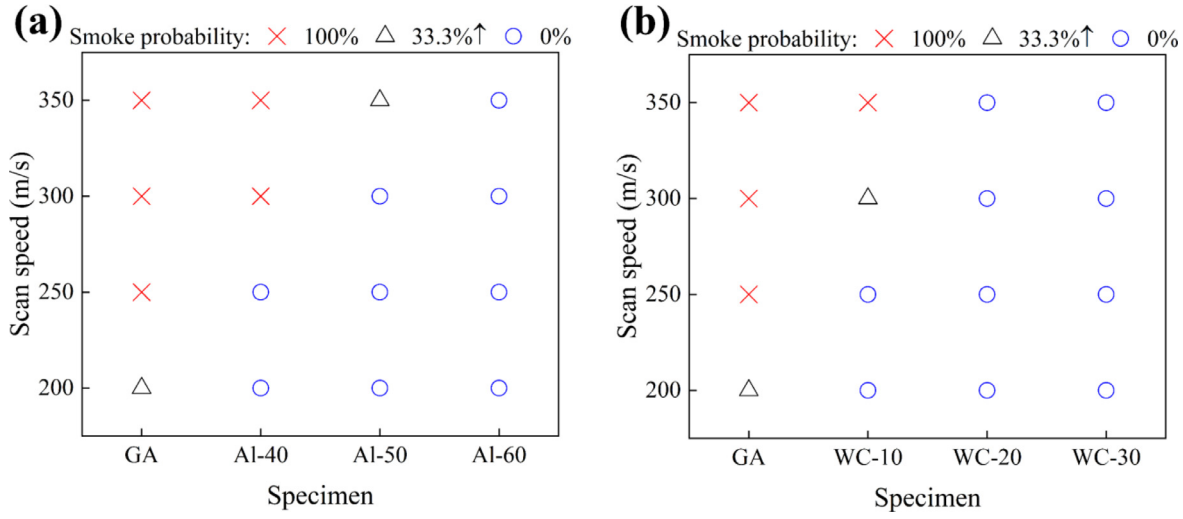

Fig. 14. Smoke probability of the Ti–48Al–2Cr–2Nb powders during the preheating process: (a) GA and Al_2O_3 ball-milled powders and (b) GA and WC ball-milled powders.

The extracted powder beds from the spreading DEM simulation are shown in Fig. 17. The clump particles were randomly distributed, and the deposited powder bed formed a network connected by individual particle contacts. The packing density of the powder bed can be calculated as

$$\rho_{PB} = \frac{V_P}{V_{voxel}} \times 100 \tag{17}$$

where V_P is the volume occupied by the particles, and V_{voxel} is the computed voxel volume. The coordination number (Z^*) of a clump particle depending on ψ_S can be calculated as follows:

$$Z^* = \frac{1}{n}\sum_{i=1}^{n}(N_{C,i} - N_{O,i}) \tag{18}$$

where $N_{C,i}$ is the total contact number of particles in clump i, $N_{O,i}$ is the contact number according to the particle overlap in merged clump i, and n is the total number of clump particles depending on ψ_S. The packing density and coordination number obtained by the DEM simulation are shown in Fig. 18. The packing density consistently increased after Al_2O_3 ball milling with increasing milling duration, and it well matched the trend of the experimental results (Fig. 18(a)). The packing density increased after WC ball milling up to WC-20 and then decreased for WC-30, which did not match the trend measured in the experiment (Fig. 18(b)). Furthermore, the coordination number of the GA powder increased with increasing milling duration. The increase in the coordination number was more rapid after WC ball milling than that after Al_2O_3 ball milling (Fig. 18(c) and (d)). This result indicates that the increase in the coordination number was not proportional to the packing density of the powder bed. The coordination numbers according to the ψ_S distribution are presented in Fig. 18(e) and (F). The general trend was that the coordination number of clump particles increased with decreasing ψ_S. Therefore, the rapid increase in the coordination number after WC ball milling was due to the increased fraction of elongated particles.

4. Discussion

4.1. Flowability and packing density of the ball-milled powders

The effect of ball milling on the packing density and flowability of the GA powder was investigated *via* coupled experiments and DEM simulations. Compared to Al_2O_3 ball milling, the flowability reduction of the GA powder was more rapid after WC ball milling, despite the shorter milling time (Fig. 7(a) and (b)). It is well known that the flowability of metallic powders is affected by the particle size, shape, and surface state [14,25,26]. Fine powders with a size of less than 45 μm can deteriorate the gravity-induced flowa-

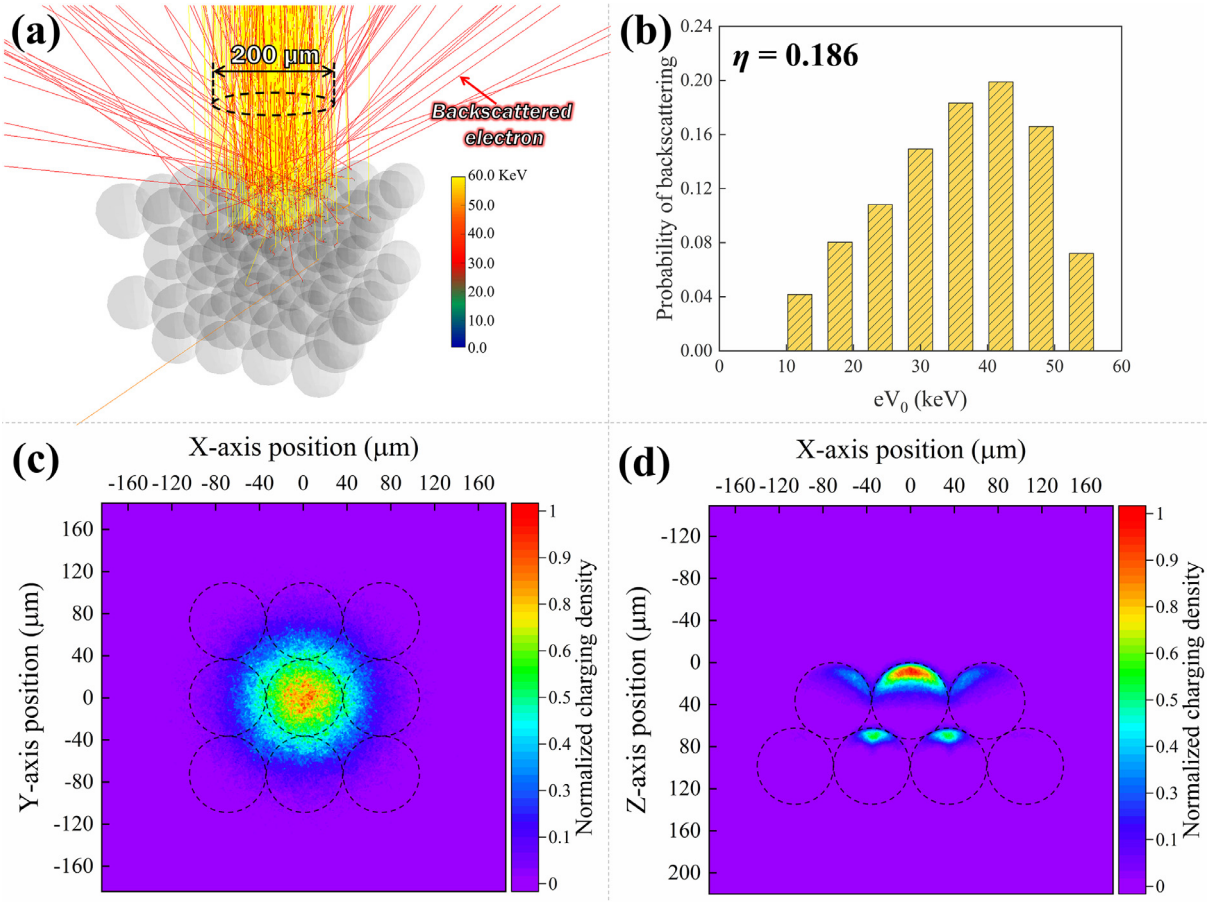

Fig. 15. Monte Carlo simulation of the smoke test of the Ti–48Al–2Cr–2Nb powder bed: (a) snapshot image colored by the acceleration voltage, (b) probability of backscattering, and electron trajectory colored by the probability density in the (c) X–Y and (d) X–Z planes.

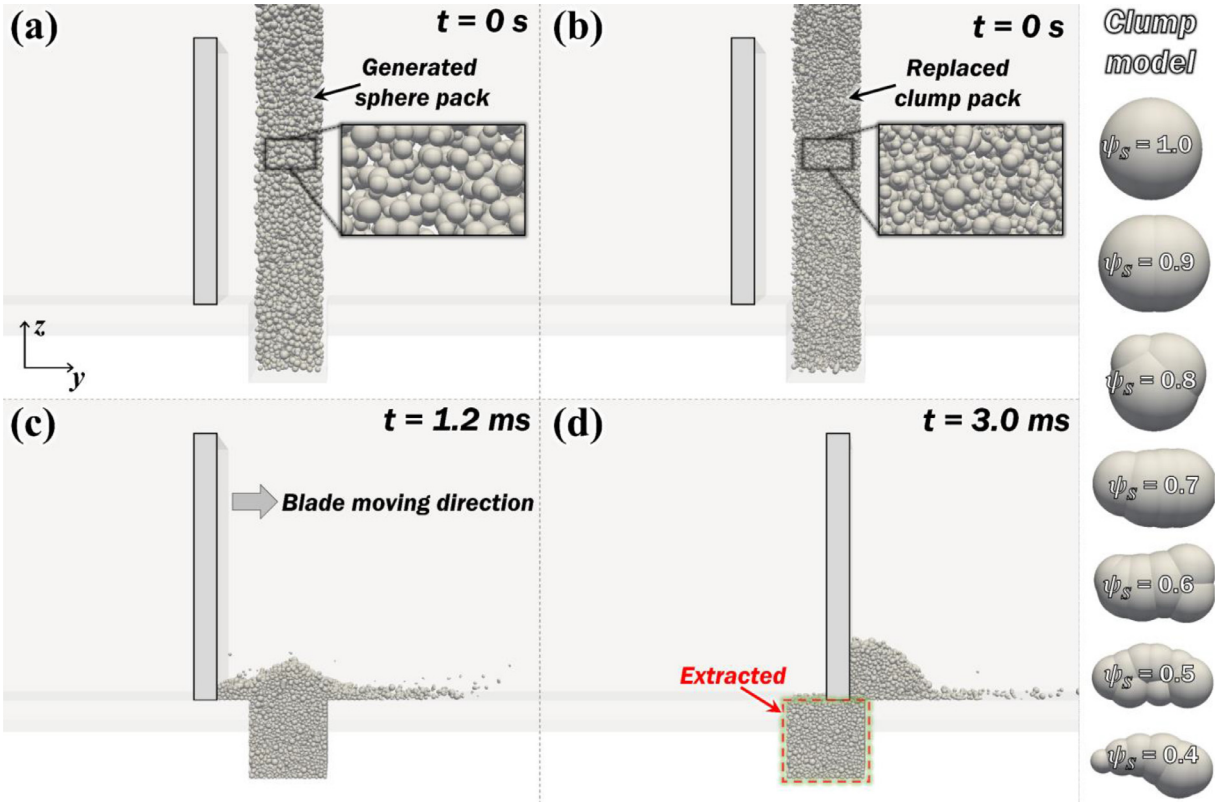

Fig. 16. Snapshot images of the spreading DEM model with the clump model: (a) sphere pack generation, (b) clump pack replacement, (c) clump pack deposition, and (d) powder spreading.

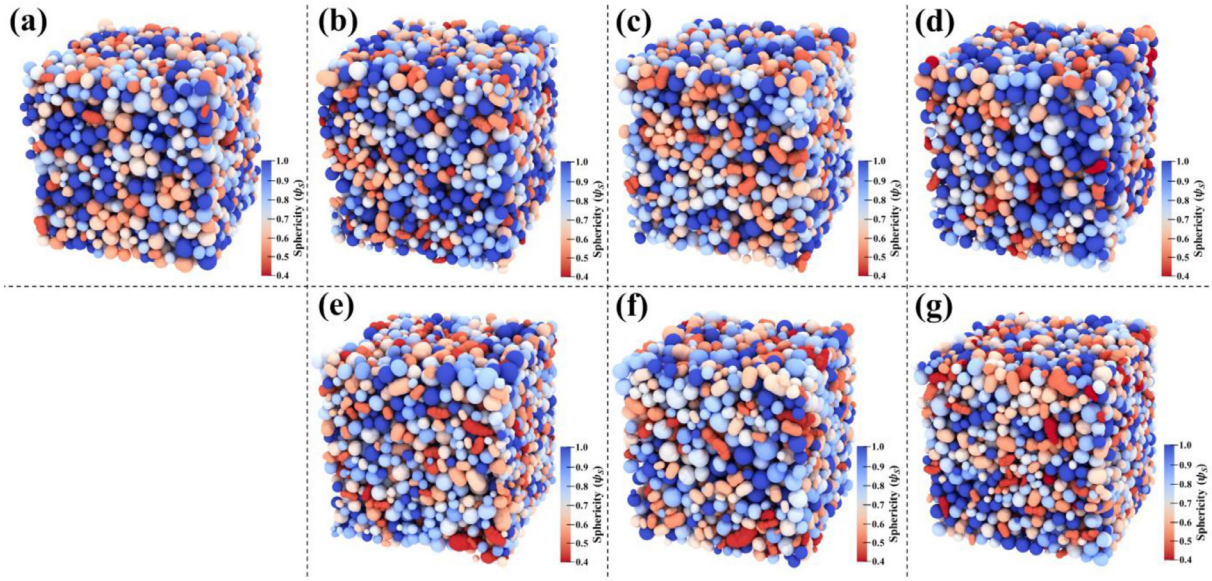

Fig. 17. Extracted powder bed of the Ti–48Al–2Cr–2Nb powders colored by sphericity: (a) GA, (b) Al-40, (c), Al-50, (d) Al-60, (e) WC-10, (f) WC-20, and (g) WC-30.

bility owing to the increased surface area and cohesive force [27]. Furthermore, the presence of elongated powders can increase interparticle friction, resulting in low flowability [28]. However, the mass flow rate of WC-10 was far lower than that of Al-60 despite their similar PSDs and fractions of elongated particles. It has been reported that the presence of angular fragments can also deteriorate the gravity-induced flowability owing to increased particle interlocking and interparticle friction [29]. As shown in Fig. 4(d) and (g), the ϕ_R broadening of WC-10 was more significant than that of Al-60, and its shape factor was higher despite the shorter milling duration. Based on the XRD and TEM observations, the GA powder mainly consisted of a lamellar microstructure comprising stacked wide α_2 + thin γ plates (Fig. 1(d) and (e)). It is well known that the α_2 phase is extremely brittle owing to limited dislocation glid in $\langle 11\bar{2}0\rangle\{10\bar{1}0\}$ systems at low temperatures [30]. From the contact mechanics simulation, the maximum contact force of the WC ball was higher than that of the Al_2O_3 ball (approximately four times), and the deformation depth was more than three times higher (Fig. 6(c)–(f)). This indicates that brittle fracture of the GA powder was favorable during WC ball milling, and the formation of angular fragments was probably owing to the high supplied contact force. Therefore, the flowability of the GA powder rapidly decreased after WC ball milling owing to the formation of angular fragments.

The packing density of the GA powder increased substantially for Al-40 after Al_2O_3 ball milling, and it gradually increased with increasing the milling duration (Fig. 7(c)). It has been suggested that a broad PSD is advantageous for obtaining a high packing density [14], whereas the presence of elongated particles can decrease the packing density through heap pore formation [31,32]. As mentioned previously, the fraction of fine particles (<60 μm) increased with increasing Al_2O_3 ball-milling duration (Fig. 3(a)), while the shape of the powder was only slightly altered (Fig. 4(c), (e), and (g)). Moreover, the attached satellites on the GA powder surface were eliminated after Al_2O_3 ball milling for 40 min (Fig. 5(a)). This indicates that the significantly increased packing density of Al-40 was due to the combined effect of the broadening of the PSD and the removal of surface satellites. Thus, the packing density increased with increasing Al_2O_3 ball-milling duration owing to PSD broadening. However, the packing density of the GA powder consistently decreased after WC ball milling despite PSD broadening and satellite removal (Fig. 7(d)). In the DEM simulation, the packing density increased up to WC-20, indicating heap pore filling through PSD broadening had a larger contribution to the packing density. This simulation result does not match the experimental results. In contrast to Al_2O_3 ball milling, the shape factor increased considerably after WC ball milling because of the formation of numerous angular fragments exhibiting irregular surfaces. This result suggests that the decrease in packing density after WC ball milling was mainly due to the formation of angular fragments, which caused local voids in the deposited powder bed. The above results demonstrate that Al_2O_3 ball milling is more suitable than WC ball milling for GA powder to obtain a high packing density with superior flowability.

4.2. Electrical properties of the ball-milled powders

The electrical properties of the GA and ball-milled powders were investigated *via* DC resistivity and AC impedance tests. The electrical resistivities of Al-40 and WC-10 decreased after ball milling, and it was decreased as increasing milling duration despite the expanded oxide film thickness (Fig. 11(a) and (b)). In the XPS results, the quantity of Ti_nO_{2n-1}-type suboxide increased in the deformed surfaces of Al-40 and WC-10, and its fraction gradually increased with increasing milling duration (Table 4). During ball milling, strain and defects can accumulate in the powder oxide film through collisions with the grinding ball and the milling vessel wall, which can even lead to the formation of amorphous phases [33]. Thus, the introduced defects in the surface oxide film can partially reduce the TiO_2 phase as follows [34]:

$$Ti_{Ti}^{4+} + O_O^{2-} \rightarrow Ti_{Ti}^{3+} + V_{\dot{o}} + e^- + \frac{1}{2}O_2(g) \quad (19)$$

where Ti_{Ti}^{4+} is a Ti^{4+} ion at a titanium site, O_O^{2-} is an O^{2-} ion at an oxygen site, Ti_{Ti}^{3+} is a Ti^{3+} ion at a titanium site, and $V_{\dot{o}}$ is a doubly ionized oxygen vacancy. Xu et al. [35] reported that Ti_nO_{2n-1}-type suboxide exhibited metal-like electrical resistance owing to the presence of ionized oxygen vacancies. Zheng et al. [36] reported that an applied tensile strain can reduce the $V_{\dot{o}}$ formation energy by the combined effect of both elastic and polaronic energy gains. Thus, the decrease in the electrical resistance of the ball-milled powders could be contributed by the synergistic effect of the accumulation of strain and defects in the oxide film, which can decrease the $V_{\dot{o}}$ formation energy, resulting in an in-

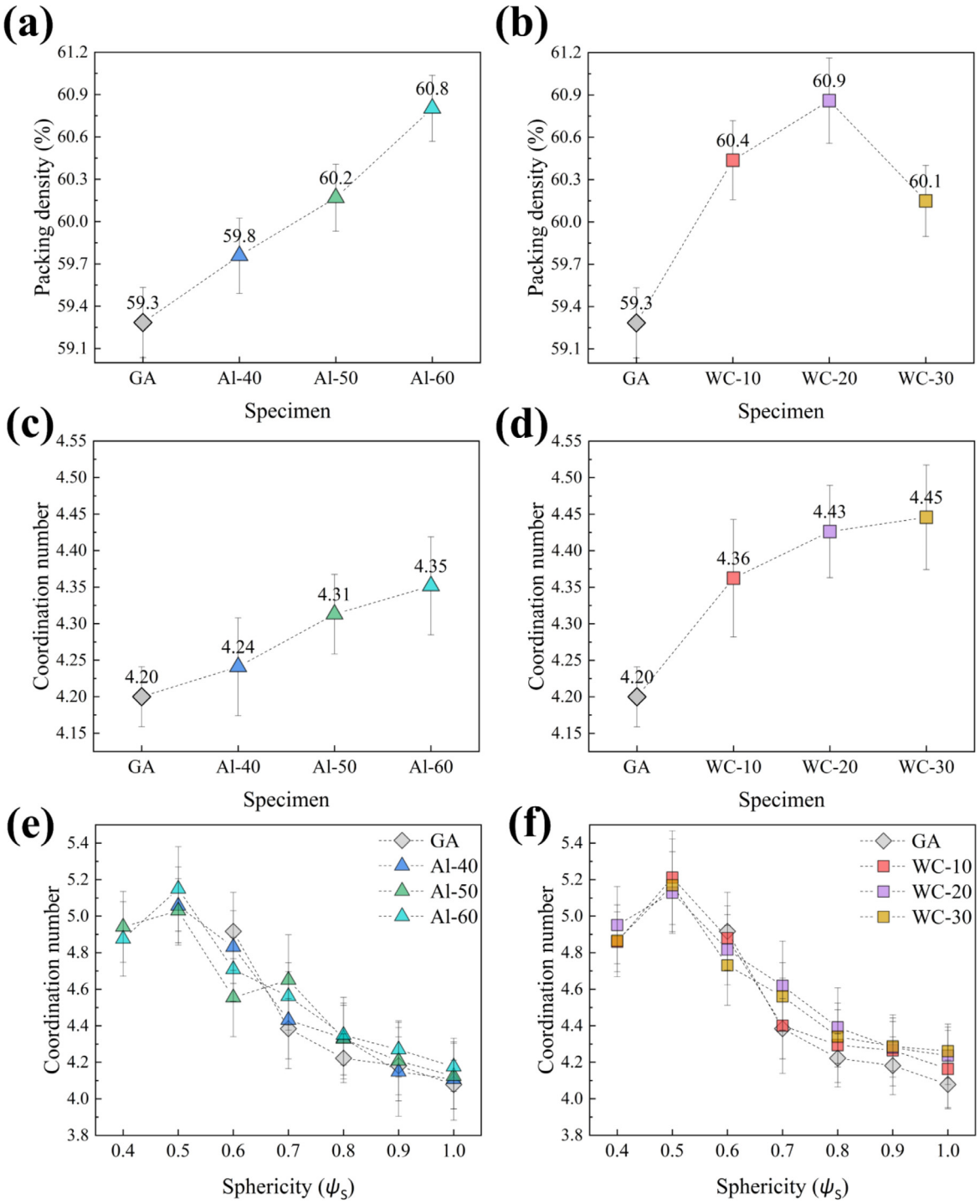

Fig. 18. Powder bed properties of the Ti–48Al–2Cr–2Nb powders: (a), (b) packing density and (c), (d), (e), (f) coordination number. (a), (c), and (e) correspond to the GA and Al_2O_3 ball-milled powders, whereas (b), (d), and (f) correspond to the GA and WC ball-milled powders.

crease in the oxygen vacancy density. Interestingly, the capacitive response of GA powder transitioned to an inductive response in Al-60 and WC-30 powders, and their valence band tails increased considerably, representing metal-like electrical conductivity (Fig. 10(a) and (b)). In the Ti *2p* spectra, the Ti^{3+} and Ti^{2+} peaks broadened, indicating the accumulation of numerous defects and considerable strain at the particle surface (Fig. 9(c) and (d)) [37]. From the TEM observations, the diffraction pattern of oxide film near the metallic matrix exhibited amorphous-like diffraction patterns in Al-60 and WC-30 owing to the fracture of crystallites by ball milling (Fig. 8(d) and (e)). Mott firstly suggested that the oxide of a 3d transition metal, which is a type of Mott insulator, can be transitioned to metal by the manipulation of temperature, pressure, doping degrees [38]. Benson et al. [39] demonstrated that the strain-induced metal–insulator transition of TiO_2 is due to the increased energy distribution of oxygen vacancies near the conduction band. Moreover, Chiba et al. [5,11] demonstrated that the thin oxide film of Inconel 718 powder can be occurred the metal-insulator transition by mechanical stimulation *via* ball milling owing to accumulated strain and defects. This result indicates that

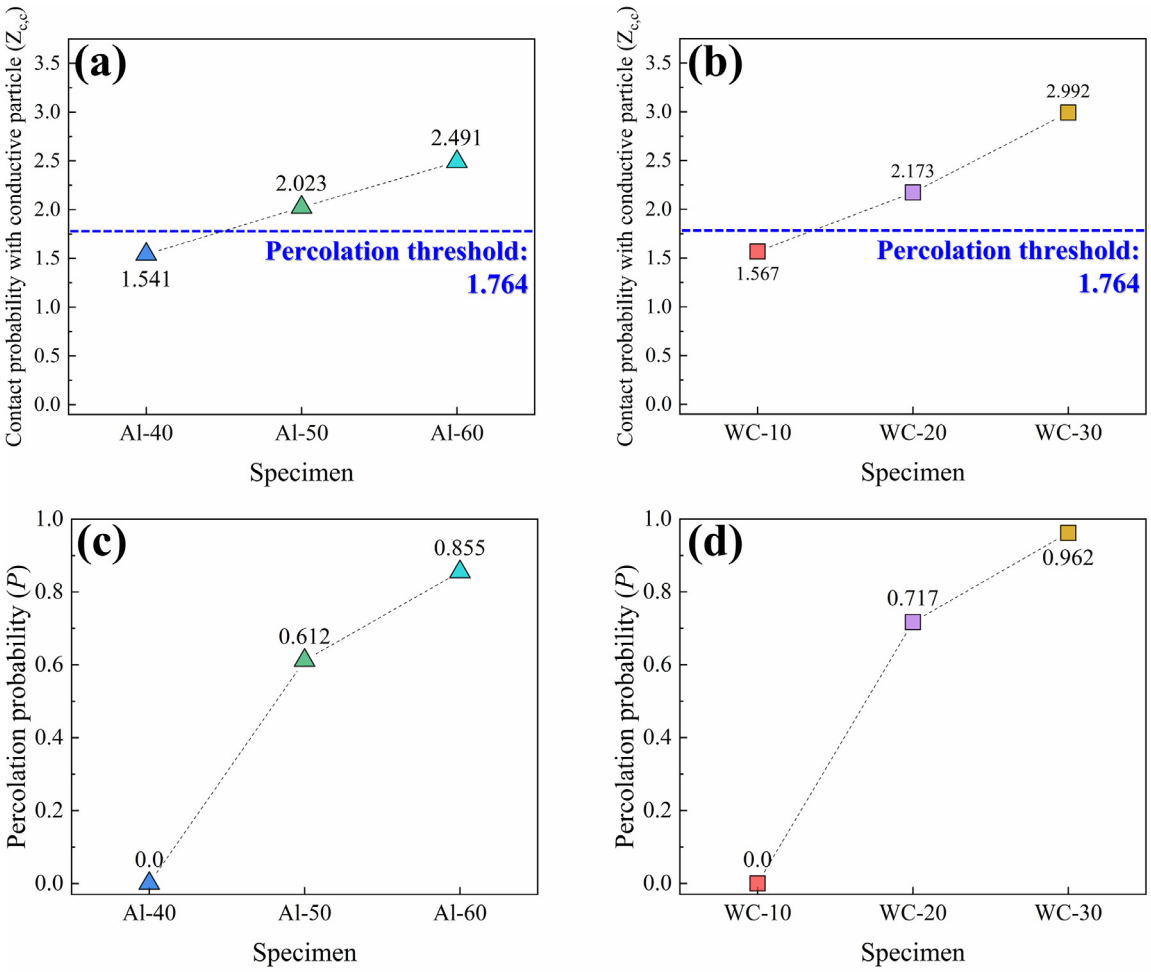

Fig. 19. Contact probability with conductive particles and percolation probability of the Ti–48Al–2Cr–2Nb powders: (a), (c) Al_2O_3 ball-milled powders and (b), (d) WC ball-milled powders.

the entire oxide film of GA powder was mechanically deformed in Al-60 and WC-30 *via* ball milling, and the accumulation of strain and defects is sufficient to cause the metal–insulator transition of the thin oxide film. Therefore, the deformed oxide films of Al-60 and WC-30 could not act as a capacitor; rather, they acted like conductive metal by the metal–insulator transition *via* mechanical stimulation.

4.3. Elucidation of the smoke mechanism

The smoke probability of the ball-milled powders during the preheating process was investigated at various scan speeds. The smoke probability of WC-10 was lower than that of Al-40 at a scan speed of 300 m/s, despite the longer charge dissipation time (Fig. 14(a) and (b)). This does not match the predicted electrostatic force based on the analytical model (Fig. 13(b)). Similarly, smoke was suppressed for WC-20 at a scan speed of 350 m/s, while smoke occurred for Al-50, despite the shorter charge dissipation time. This result indicates that the charge dissipation time measured by the impedance test cannot fully predict the powder bed smoke tendency during the preheating process. From the electron trajectory simulation, most of the electrons lose their kinetic energy and are trapped in the powder within a penetration depth of 90 μm (Fig. 15(d)). Therefore, the contact state between the powders can significantly affect the electrical charging of the powder bed because the irradiated charges should be transferred through the connected network of individual powder particles into the base plate. In the deposited powder bed, the possible transfer paths of the electrical current increase with increasing coordination number of the powder [40,41]. As mentioned previously, the chemical compositions of the deformed surfaces in the powders with τ values on the same scale, such as Al-40 and WC-10, Al-50 and WC-20, and Al-60 and WC-30, were nearly identical (Table 4). Assuming that the deformed surface properties are the same for powders with τ values on the same scale, the contact probability with the conductive particles ($Z_{c,c}$) can be expressed as [42]

$$Z_{c,c} = Z^* \cdot f_d \tag{20}$$

Based on percolation theory, the percolation probability (P) of the powder bed can be expressed as [43]

$$P = \left(1 - \left(\frac{3.764 - Z_{c,c}}{2}\right)^{2.5}\right)^{0.4} \tag{21}$$

Thus, the threshold of $Z_{c,c}$ for percolation was determined to be 1.764. The calculated $Z_{c,c}$ and P values of the ball-milled powders are presented in Fig. 19. The $Z_{c,c}$ value of WC-10 was higher than that of Al-40, indicating more possible paths for charges to pass through the conductive particles. Moreover, the ϕ_R broadening of WC-10 was more significant than that of Al-40, and its shape factor was considerably higher, indicating irregular particle surfaces (Fig. 4(c) and (d)). Jennings et al. [44] reported that the maximum coordination number increases with increasing irregularity of particles owing to the increased probability of multiple contacts with

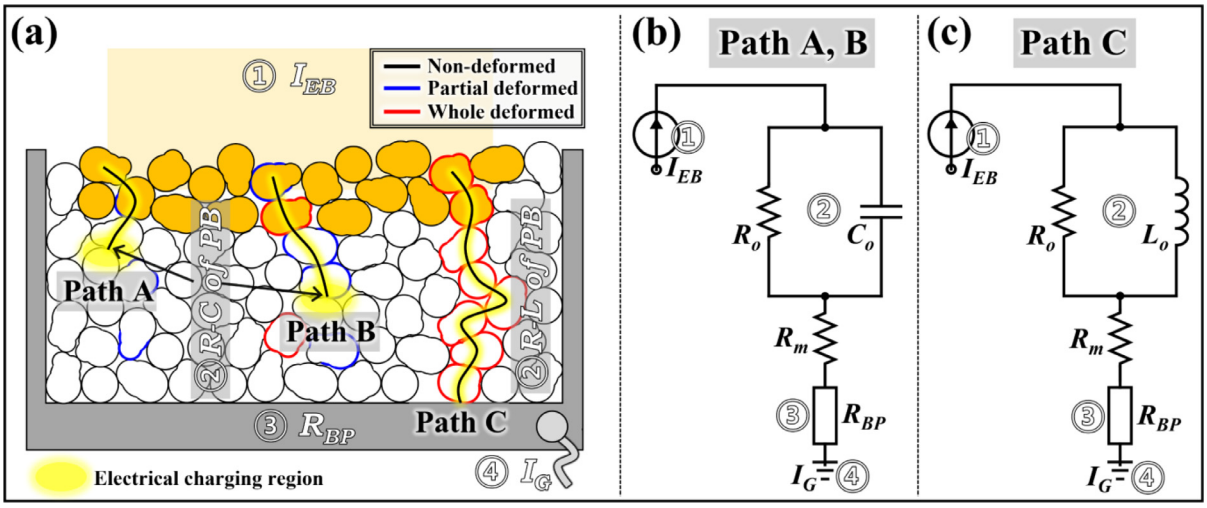

Fig. 20. (a) Schematic of possible charge conduction paths through the powder bed during the preheating process and corresponding equivalent electrical circuits: (b) resistor–capacitor and (c) resistor–inductor.

neighboring particles. Thus, it can be deduced that the coordination number of the WC-10 powder bed was higher than that of the Al-40 powder bed owing to the multiple contacts of particles with irregular surfaces. Therefore, the occurrence of smoke during the preheating process was more difficult for WC-10 than that of Al-40 because of the rapid charge dissipation through the conductive particles. However, the $Z_{c,c}$ values of Al-40 and WC-10 were lower than the percolation threshold of 1.764. Thus, the charges supplied to Al-40 and WC-10 should transfer through the insulating oxide film acting as a capacitor, and smoke should occur at scan speeds above 300 m/s owing to limited charge redistribution. The $Z_{c,c}$ value of WC-20 was higher than that of Al-50, and these values were higher than the percolation threshold. This indicates that the smoke probability of WC-20 should be lower than that of Al-50 because of the rapid charge dissipation through the contacting conductive particles. However, in the impedance test, a capacitive response was observed for Al-50 and WC-20 owing to the insufficient accumulation of strain and defects in the oxide film (Fig. 12(b) and (F)). Therefore, smoke would occur for Al-50 and WC-20 under certain conditions despite the increased percolation probability owing to the capacitive behavior of oxide film. As the milling duration increased, sufficient defects and strain were accumulated on oxide film for Al-60 and WC-30, and a capacitive response was altered to inductive response, which directly proves the metal-like electrical conductivity, *via* metal–insulator transition. Moreover, the percolation probabilities of Al-60 and WC-30 increased to 0.846 and 0.977, respectively (Fig. 19(c) and (d)). Therefore, smoke can be effectively suppressed for Al-60 and WC-30 through the formation of a conductive percolation cluster exhibiting metal-like electrical conductivity.

Finally, a schematic of the possible charge conduction paths through the powder bed during the preheating process is presented in Fig. 20. In the Al-40 and WC-10 powders, the oxide film was partially deformed, and $Z_{c,c}$ was lower than the percolation threshold. Thus, powder bed smoke can occur owing to the restricted charge redistribution, as shown in Path A in Fig. 20(a). In the Al-50 and WC-20 powders, the deformed area and coordination number increased, and their $Z_{c,c}$ values were higher than the percolation threshold. However, the oxide film on the partially deformed particle surface exhibited capacitive behavior owing to insufficient strain and defect density. Thus, electrical charges can accumulate on the powder bed, and smoke can occur under certain conditions, as shown in Path B in Fig. 20(a). Therefore, the equivalent electrical circuit of Paths A and B in the PBF-EB building process is a resistor–capacitor circuit, as shown in Fig. 20(b). In the Al-60 and WC-30 powders, the entire oxide film was mechanically deformed, and it acted like a metal *via* metal–insulator transition because of the sufficient strain and defect density in the oxide film. Moreover, the percolation probabilities of Al-60 and WC-30 were higher than 0.846 because of the increased coordination number and deformed area. Therefore, powder bed smoke was completely suppressed by the formation of a percolation cluster exhibiting metal-like electrical conductivity, as shown in Path C in Fig. 20(a). Furthermore, the equivalent electrical circuit of Path C in the PBF-EB building process is determined to be a resistor–inductor circuit, as shown in Fig. 20(c). Based on the above results, we can conclude that the most desirable powder feedstock for PBF-EB is the Al-60 powder, which exhibited a high packing density and good smoke suppression during the preheating process.

5. Conclusions

In this study, the influence of mechanical stimulation using the Al_2O_3 and WC ball milling on the electrical and powder bed properties of gas-atomized Ti–48Al–2Cr–2Nb was investigated. Furthermore, the smoke mechanism of ball-milled powders was elucidated based on percolation theory using experimental and simulation results. The conclusions of this study are as follows:

(1) Gas-atomized Ti–48Al–2Cr–2Nb was mechanically ball-milled for up to 60 min using Al_2O_3 and WC balls. Compared to that after Al_2O_3 ball milling, PSD widening was more extensive after WC ball milling, despite the shorter milling duration. The formation of angular fragments was more favorable after WC ball milling than that after Al_2O_3 ball milling owing to the high impact force originated by heavy weight. Moreover, the formation of angular fragments by WC ball milling significantly reduced the flowability and packing density due to increased particle interlocking and residual pores.

(2) The electrical properties of the ball-milled powders were characterized *via* DC resistivity and AC impedance tests. The electrical resistivity of the GA powder gradually decreased with increasing ball-milling duration despite the increased oxide film thickness. This could be due to the accumulation of strain and defects promoting the Ti_nO_{2n-1}-type suboxide in the surface oxide film *via* ball milling. The capacitive response in Al-60 and WC-30 was replaced by an inductive response representing metal-like electrical conductivity. This could be due to the

metal–insulator transition of deformed oxide film caused by the accumulation of sufficient stain and defects *via* ball milling.

(3) The smoke probability during the preheating process was investigated using the pulse repetition method. Smoke was more suppressed for WC-10 than that for Al-40, despite the longer charge dissipation time. This could be due to the high contact probability with conductive particles, which provided rapid charge dissipation paths. Smoke was further suppressed for Al-50 and WC-20 owing to the decreased charge dissipation time and increased $Z_{c,c}$. However, smoke occurred for Al-50 and WC-20 under certain conditions owing to charge accumulation due to the capacitive behavior of oxide film. The powder bed smoke was completely restricted for the Al-60 and WC-30 because of the formation of a percolation cluster with metal-like electrical conductivity.

In conclusion, the Al-60 powder is the most desirable powder feedstock for PBF-EB owing to its high packing density and good smoke suppression.

Acknowledgements

This work was partially supported by JSPS KAKENHI (grant numbers 18H03834 and 21k14432). This research was also supported by “Materials Integration for Revolutionary Design System of Structure Materials” of the Cross-Ministerial Strategic Innovation Promotion Program (SIP) of Japan Science and Technology (JST). This work was also based on the results obtained from a project commissioned by the New Energy and Industrial Technology Development Organization (NEDO) (JPNP14014). This work was partly supported by the Technology Research Association for Future Additive Manufacturing (TRAFAM). This work is also based on the results obtained from a project (JPNP19007) commissioned by the New Energy and Industrial Technology Development Organization (NEDO).

References

[1] A. Gisario, M. Kazarian, F. Martina, M. Mehrpouya, J. Manuf. Syst. 53 (2019) 124–149.
[2] Y. Lei, K. Aoyagi, K. Aota, K. Kuwabara, A. Chiba, Acta Mater. 208 (2021) 116695.
[3] V. Juechter, M.M. Franke, T. Merenda, A. Stich, C. Körner, R.F. Singer, Addit. Manuf. 22 (2018) 118–126.
[4] A. Takase, T. Ishimoto, R. Suganuma, T. Nakano, Addit. Manuf. 47 (2021) 102257.
[5] A. Chiba, Y. Daino, K. Aoyagi, K. Yamanaka, Materials 14 (2021) 4662.
[6] T. Kim, J.M. Oh, G.H. Cho, H. Chang, H.D. Jang, J.W. Lim, Appl. Surf. Sci. 534 (2020) 147623.
[7] Z.C. Cordero, H.M. Meyer, P. Nandwana, R.R. Dehoff, Acta Mater. J. 124 (2017) 437–445.
[8] H.B. Qi, Y.N. Yan, F. Lin, W. He, R.J. Zhang, Proc. Inst. Mech. Eng. Part 220 (2006) 1845–1853.
[9] M. Sigl, S. Lutzmann, M.F. Zaeh, in: 17th Solid Free. Fabr. Symp. SFF 2006, 2006, pp. 464–477.
[10] C. Eschey, S. Lutzmann, M.F. Zaeh, in: 20th Annu. Int. Solid Free. Fabr. Symp. SFF 2009, 2009, pp. 308–319.
[11] S. Yim, H. Bian, K. Aoyagi, K. Yanagihara, S. Kitamura, H. Manabe, Y. Daino, Y. Hayasaka, K. Yamanaka, A. Chiba, Addit. Manuf. 51 (2022) 102634.
[12] A. Bor, B. Jargalsaikhan, J. Lee, H. Choi, Coatings 10 (2020) 1–15.
[13] L. Zhang, Z. Huang, Y. Liu, Y. Shen, K. Li, Z. Cao, Z. Ren, Y. Jian, Materials 12 (2019) 1–17.
[14] S. Yim, H. Bian, K. Aoyagi, K. Yamanaka, A. Chiba, Addit. Manuf. 49 (2022) 102489.
[15] H. Wadell, J. Geol. 43 (1935) 250–280.
[16] P. Råback, M. Malinen, CSC-IT Cent. Sci. (2016) 1–10.
[17] Q.J. Wang, D. Zhu, in: Q.J. Wang, Y.-W. Chung (Eds.), Hertz Theory: Contact of Spherical Surfaces, Encycl. Tribol, Springer US, Boston, MA, 2013, pp. 1654–1662.
[18] V. Smilauer, E. Catalano, B. Chareyre, Yade Documentation 2nd Ed, The Yade Project, 2015.
[19] A.I. Gusev, A.S. Kurlov, Nanotechnology 19 (2008) 265302.
[20] M.J. Blackburn, in: Technology and Application of Titanium, Pergamon, 1970, pp. 633–643.
[21] J.F. Moulder, J. Chastain, Handbook of X-Ray Photoelectron Spectroscopy: A Reference Book of Standard Spectra for Identification and Interpretation of XPS Data, Physical Electronics Division, Perkin-Elmer Corporation, 1992.
[22] Y. Shao, J. Li, Y. Li, H. Wang, Q. Zhang, R.B. Kaner, Mater. Horizons 4 (2017) 1145–1150.
[23] E. Von Hauff, J. Phys. Chem. C 123 (2019) 11329–11346.
[24] R. Gauvin, G. L'Espérance, J. Microsc. 168 (1992) 153–167.
[25] L. Cordova, T. Bor, M. de Smit, M. Campos, T. Tinga, Addit. Manuf. 32 (2020) 101082.
[26] Y. Zhao, Y. Cui, Y. Hasebe, H. Bian, K. Yamanaka, K. Aoyagi, T. Hagisawa, A. Chiba, Powder Technol. 393 (2021) 482–493.
[27] N. Vlachos, I.T.H. Chang, Powder Technol. 205 (2011) 71–80.
[28] L. Haferkamp, L. Haudenschild, A. Spierings, K. Wegener, K. Riener, S. Ziegelmeier, G.J. Leichtfried, Metals 11 (2021) 1–14.
[29] H.M. Beakawi Al-Hashemi, O.S. Baghabra Al-Amoudi, Powder Technol. 330 (2018) 397–417.
[30] S. Yim, H. Bian, K. Aoyagi, A. Chiba, Mater. Sci. Eng. A 816 (2021) 141321.
[31] S. Haeri, Y. Wang, O. Ghita, J. Sun, Powder Technol. 306 (2017) 45–54.
[32] G.T. Nolan, E. Kavanagh, Powder Technol. 78 (1994) 231–238.
[33] S. Yim, I. Park, J. Park, Ceram. Int. 44 (2018) 14044–14052.
[34] R. Amade, P. Heitjans, S. Indris, M. Finger, A. Haeger, D. Hesse, J. Photochem. Photobiol. A 207 (2009) 231–235.
[35] X. Baoqiang, H.Y. Sohn, Y.M.A.Y. Lan, RSC Adv. 9 (2016) 79706–79722.
[36] Y.F. Zheng, S. Chen, J.H. Yang, X.G. Gong, Phys. Rev. B 99 (2019) 1–6.
[37] B.C. Beard, H.W. Sandusky, B.C. Glancy, W.L. Elban, Surf. Interface Anal. 20 (1993) 140–148.
[38] N.F. Mott, Pure Appl. Chem. 52 (1980) 65–72.
[39] E.E. Benson, M.A. Ha, B.A. Gregg, J. van de Lagemaat, N.R. Neale, D. Svedruzic, Sci. Rep. 9 (2019) 1–8.
[40] K. Bourbatache, M. Guessasma, E. Bellenger, V. Bourny, A. Tekaya, Granul. Matter. 14 (2012) 1–10.
[41] F. LUX, J. Mater. Sci. 28 (1993) 285–301.
[42] C. Zhai, Y. Gan, J. Coupled Syst. Multiscale Dyn. 6 (2019) 310–316.
[43] D. Chen, Z. Lin, H. Zhu, R.J. Kee, J. Power Sources 191 (2009) 240–252.
[44] C. Jennings, M. Ramsay, T. Hudson, P. Harrowell, Mol. Phys. 113 (2015) 2755–2769.